Building Efficient Light-Matter Interfaces for Quantum Systems

by

Tsung-Ju Jeff Lu

B.S. Electrical Engineering, California Institute of Technology (2013)

Submitted to the Department of Electrical Engineering and Computer Science
in partial fulfillment of the requirements for the degree of

Master of Science in Electrical Engineering and Computer Science

at the

MASSACHUSETTS INSTITUTE OF TECHNOLOGY

September 2015

Author ..... Signature redacted .....
Department of Electrical Engineering and Computer Science
August 28, 2015

Certified by.... Signature redacted .....
Dirk R. Englund
Assistant Professor of Electrical Engineering
Thesis Supervisor

Accepted by ..... Signature redacted .....
Professor Leslie A. Kolodziejski
Chair of the Committee on Graduate Students

Building Efficient Light-Matter Interfaces for Quantum Systems

by

Tsung-Ju Jeff Lu

Submitted to the Department of Electrical Engineering and Computer Science
on August 28, 2015, in partial fulfillment of the
requirements for the degree of
Master of Science in Electrical Engineering and Computer Science

Abstract

Efficient collection of photons from quantum memories, such as quantum dots (QDs) and nitrogen vacancy (NVs) centers in diamond, is essential for various quantum technologies. This thesis describes the design, fabrication, and utilization of novel photonic structures and systems to achieve potentially world-record photon collection from quantum dots. This technique can also be applied to NVs in diamond in the near future.

Also, the NV^- charged state has second-scale coherence times at room temperature that make it a promising candidate for solid state memories in quantum computers and quantum repeaters. NV^- is an individually addressable qubit system that can be optically initialized, manipulated, and measured. On-chip entanglement generation would be the basis of scalability for quantum information processing technologies. These properties have enabled recent demonstrations of heralded quantum entanglement and teleportation between two separated NV centers. To improve the entanglement probability in such schemes, it is imperative to improve the efficiency with which single photons from a NV center can be guided into a low-loss single-mode waveguide. As such, a second component of this thesis focuses on the development of a photonic integrated circuit based on aluminum nitride that would incorporate pre-selected, long-lived NV center quantum memories as well as pre-selected, high-performance superconducting nanowire single-photon detectors (SNSPDs). This hybrid device would have the capability to perform on-chip entanglement of photons from separate quantum memories to build up a quantum repeater necessary for long-distance quantum communication and distributed quantum computing.

Thesis Supervisor: Dirk R. Englund
Title: Assistant Professor of Electrical Engineering

Acknowledgments

This thesis would not have been possible without the guidance of many people. First of all, I would like to acknowledge my advisor, Professor Dirk Englund, for his guidance and support. It has been a real privilege to work with Professor Englund, learning directly from him, and always being able to ask him for advice on anything. He has played such a large role in shaping my academic and research interests and helping me reach my goals that I would like to thank him for that.

I would also like to thank everyone in the Quantum Photonics Laboratory for their help in everything. I have truly learned so much in the past two years from everyone in the group. I feel like I am a better researcher and person as a result. It is amazing to work with this group of highly intelligent and extremely motivated academics. It is really a blessing to be in such a wonderful work environment. I particularly want to thank Dr. Gabriele Grosso for helping me with the fiber-integrated single photon source project in this thesis. He worked with me on building the optical setup and mentored me in doing the spectroscopy experiments.

Also, I would like to thank my collaborators Ryan Camacho, Matt Eichenfield, Ian Frank, and Jeremy Moore from Sandia National Laboratories. Although I only visited for one week, it was a great experience to see what it was like to work in a national lab. I appreciated all of you making me feel welcomed. I enjoyed Albuquerque very much and look forward to visiting more in the future for our collaboration.

In addition, I would like to thank Jim Daley and Mark Mondol of NanoStructures Laboratory for all their help and expertise in fabrication. Furthermore, I would like to thank Eric Lim, Dave Terry, Bob Bicchieri, and the rest of Microsystems Technology Laboratories for all their help and expertise in fabrication as well. Developing a reliable fabrication process was a difficult part in this Master's Thesis, so I am grateful to all these people for helping me with this huge obstacle.

Finally, I want to give my utmost thanks to my mother and father for their love, care, and countless sacrifice they have made for my education. They have been my guiding light in every difficult and important decision throughout my life. They are

very supportive in everything I do, and I live to make them proud. Thank you so much for being the best parents imaginable.

Contents

List of Figures

Chapter 1

Introduction

1.1 Self-assembled semiconductor quantum dots

On-demand single photon sources are necessary for many quantum technologies, particularly quantum key distribution, where it is imperative to have single photons with known polarizations. On-demand single photon sources also have applications in quantum computation using only linear optics, as well as quantum repeaters for quantum optical communication. Typically, on-demand single photon sources involve a dipole transition in a two-level quantum system. Self-assembled epitaxially-grown semiconductor quantum dots (QDs) are one of the best candidates for on-demand single photon sources today since about 90% of the photons emitted from it are emitted in the zero-phonon line. Also, they have good multi-photon suppression, as well as quantum-mechanically indistinguishability between consecutive photons. In the case of self-assembled semiconductor quantum dots, a charged carrier decays from a high-energy state to a low-energy state and releases a single photon in the process with wavelength $\frac{hc}{\Delta E}$, where ΔE is the energy difference between the two energy levels.

A quantum dot is a nanometer-sized semiconductor nanocrystal that confines charge carriers (excitons) in all directions and in a small volume (around the same order in size as the exciton Bohr radius or smaller); it needs to be small enough so that the excitons can interact. They behave as artificial atoms that exhibit quantum mechanical properties and have well-defined energy levels. The quantum confinement

of electron-hole pairs (excitons) and electrostatic interaction between electrons and holes inside the quantum dot result in a discrete spectrum. It is easy to tune the emission wavelength of a quantum dot during fabrication. The larger the quantum dot, the larger the emission wavelength. However, one cannot simply increase the size of a quantum dot indefinitely either since it needs to be small enough to be in the strong confinement regime so that the optical properties are tunable. The exciton Bohr radius is given by:

$$a_b^* = \varepsilon_r \left(\frac{m}{\mu} \right) a_b \tag{1.1}$$

where a_b is the Bohr radius (which is material dependent), m is the mass, μ is the reduced mass, and ε_r is the size-dependent dielectric constant.

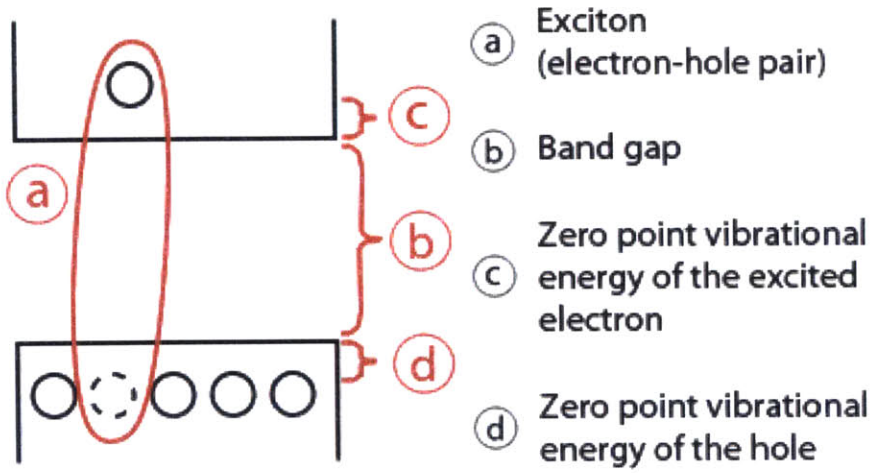

Figure 1-1: Simplified depiction of the excited electron and the hole in an exciton entity and the corresponding energy levels. The total energy is the sum of the band gap energy between the occupied level and unoccupied energy level, the energy involved in the Coulomb attraction in the exciton, and the confinement energies of the excited electron and the hole [24].

As shown in Figure 1-1, to make the quantum dot fluoresce, an electron is first excited to the conduction band, usually by photo-pumping with a laser with lower wavelength than the band gap. This leaves behind a hole in the valence band. Then

fluorescence is achieved when the excited electron relaxes to the ground state and combines with a hole. The emitted photon energy E is the sum of:

1. The band gap energy $E_{bandgap}$ between the occupied level and the unoccupied energy level.

2. Confinement energies of the hole and the excited electron. Since the exciton in a quantum dot can be treated as a particle in a box, the confinement energy of the exciton can be varied by changing the quantum dot size:

$$E_{confinement} = \frac{\hbar^2\pi^2}{2a^2}\left(\frac{1}{m_e} + \frac{1}{m_h}\right) = \frac{\hbar^2\pi^2}{2\mu a^2} \tag{1.2}$$

   where a is the radius, m_e is the electron mass, m_h is the hole mass, and μ is the reduced mass.

3. Bound energy of the exciton, which is a bound state of an electron and a hole held together by attractive electrostatic Coulomb forces:

$$E_{exciton} = -\frac{1}{\varepsilon_r^2}\frac{\mu}{m_e}R_y = -R_y^* \tag{1.3}$$

   where ε_r is the size-dependent dielectric constant, μ is the reduced mass, m_e is the free electron mass, and $R_y = 13.6eV$ is the Rydberg constant.

In summary, the emitted photon energy E is given by the following equation, which shows that the luminescence is typically red-shifted with respect to the excitation light and varying the size of the quantum dot can tune the emission energy:

$$\begin{aligned} E &= E_{bandgap} + E_{confinement} + E_{exciton} \\ &= E_{bandgap} + \frac{\hbar^2\pi^2}{2\mu a^2} - R_y^* \end{aligned} \tag{1.4}$$

For this thesis, I will be using Indium Arsenide (InAs) quantum dots epitaxially grown on Gallium Arsenide (GaAs). Specifically, the quantum dots are created using self-assembled growth by Stransky-Krastanov molecular beam epitaxy. The

self-assembly growth leads to variations in size of the quantum dots and variations in the InGaAs composition, which causes an inhomogeneous distribution of emission wavelength. Physically, the quantum dots are disk-like shaped with dimensions of about 5nm tall and 20 to 40nm in diameter. Since the transitions are influenced by the QD size, QD height, and InGaAs composition, these quantum dots usually emit single photons with wavelength around 940nm, with a FWHM of around 20-30nm.

1.1.1 Progress and Challenges of Using Epitaxial Quantum Dots

Even with all the advancements in harnessing epitaxial quantum dots as on-demand single photon sources, the efficient extraction of light is still a big challenge today and is essential for many applications in quantum information processing. The emitted single photons from QDs suffer from total internal reflection at the semiconductor-air interface since epitaxial quantum dots are embedded in semiconductor material. Previous attempts at surmounting this problem include micropillar [21] cavities and photonic crystal cavities [8]. However, this requires spectral tuning of the cavity resonance to the QD emission line. Bulk epitaxial quantum dots have a broadband spectrum, so spectral tuning of the cavity resonance to a QD that is spatially aligned to a cavity center is very difficult. Being able to develop a system that is operational for broadband wavelengths while offering Purcell enhancement for improving photon collection would help create the ideal on-demand single photon source.

1.2 Nitrogen Vacancy Center in Diamond

1.2.1 NV^- defect center

The nitrogen vacancy (NV) color defect center in diamond has been the subject of intense research efforts in recent years because it is fluorescent and has unique spin properties. Specifically, the singly negatively charged NV^- center is a promising candidate for solid state spin qubit in quantum information processing [7, 16]. The

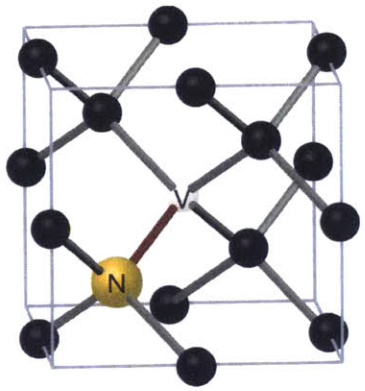

Figure 1-2: Schematic of the nitrogen vacancy center in the diamond lattice.

NV defect center consists of a substitutional nitrogen atom and neighboring vacancy in the diamond lattice (Figure 1-2) [9]. It has two fluorescent charge states NV^- and NV^0. The NV^- has a ground state spin triplet that is promising for numerous applications while the NV^0 is less studied and is generally considered undesirable. The two charge states have distinct electronic structure and therefore different fluorescence intensities as well as spectra.

Researchers around the world have demonstrated various quantum technologies, including quantum entanglement [23], teleportation [18], and sensing [22], by taking advantage of the unequaled optical and spin properties of NVs in diamond. In order to achieve faster quantum information processing [3] and better sensitivity in metrology, it is necessary to have efficient routing and detection of the NV photoluminescence. Typically, the total internal reflection confinement due to the high refractive index of diamond limits efficient photon collection. Previous attempts at this challenge in bulk diamond use techniques such as vertical pillars [2], solid immersion lenses, photonic crystal cavities [19], etc. to achieve photon collection rates of about one million counts per second. Being able to push this number far beyond that offered by current technology is important for performing single shot readout of NVs at room temperature.

1.3 Thesis Outline

Efficient collection of photons from quantum memories, such as quantum dots and nitrogen vacancy centers in diamond, is essential for various quantum technologies. This thesis shows efforts toward this by integrating a "bullseye" circular grating structure for quantum dots onto a fiber facet, which can also be extended to NVs in diamond [12, 1]. Doing so would take advantage of the lower index contrast of the diamond- (semiconductor-) glass interface compared to the diamond- (semiconductor-) air interface to have preferentially most of the dipole emission emitting into the fiber. Integrating these quantum emitters directly onto optical fibers would eliminate collection loss in unnecessary free-space optical components [17]. Also, it would achieve a compact system that can be a plug-and-play for quantum information processing applications.

In addition, the NV^- nuclear spin state has second-scale coherence times at room temperature that makes it a promising candidate for solid state memories in quantum computers and quantum repeaters [13]. NV^- is an individually addressable qubit system that can be optically initialized, manipulated, and measured [6]. On-chip entanglement generation would be the basis of scalability for quantum information processing technologies. These properties have enabled recent demonstrations of heralded quantum entanglement and teleportation between two separated NV centers [3]. To improve the entanglement probability in such schemes, it is imperative to improve the efficiency with which single photons from an NV center can be guided into a low-loss single-mode waveguide. As such, a second portion of my master's thesis would be to develop and build up a photonic integrated circuit based on aluminum nitride [26] that would incorporate pre-selected, long-lived NV center quantum memories [14] as well as pre-selected, high-performance superconducting nanowire single-photon detectors (SNSPDs) [15]. This hybrid device would have the capability to perform on-chip entanglement of photons from separate quantum memories to build up a quantum repeater necessary for long-distance quantum communication.

Chapter 2

Fiber-Integrated Single Photon Source

2.1 Motivation and Goals

The motivation for this portion of my thesis is that the single-photon rate of epitaxial QDs is limited by collection efficiency, rather than generation rate. The high refractive index contrast between GaAs ($n = 3.4$) and air causes the collection efficiency to be $< 1\%$. Photonic crystals have been shown to offer radiative rate enhancement for efficient outcoupling, as well as improved single photon rate and photon indistinguishability. However, the drawback of using photonic crystals is that high Q factor means narrow spectral band, which makes it difficult to both spectrally and spatially line up a quantum dot to a photonic crystal cavity. We propose to utilize a bullseye microcavity for broadband efficient photon extraction. As such, the goal for this portion is to demonstrate efforts toward fiber-integration of bullseye structures using pick-and-place. This would obviate an optical setup for photon extraction from QDs. We envision this system to be a potential plug-and-play device that can be placed in a cryostat, with the excitation and collection using the same access fiber.

2.2 Bullseye Grating Structure

2.2.1 Previous Studies

The bullseye microcavity structure was first introduced by Davanco et al. in 2011 [5]. It is based on high-contrast second-order Bragg gratings, where the period is equal to the guided wave wavelength:

$$\Lambda = \lambda_{QD}/n_{TE} \tag{2.1}$$

where λ_{QD} is the emission wavelength of the quantum dot and n_{TE} is the GaAs slab TE mode effective index.

This structure favors vertical light extraction that would have otherwise radiated into slab-guided modes. These periodic bullseye structures create a cavity resonance, which is caused by partial reflections at the gratings toward the center. Furthermore, the large index contrast at trenches results in strong reflections and out-of-plane scattering. Davanco et al. showed by using a far-field polar plot for the cavity mode that the collection efficiency is 53% for NA = 0.42 objective. In addition, the emitted field is nearly Gaussian and contained within 20° half-angle.

2.2.2 Pick-and-Place Method

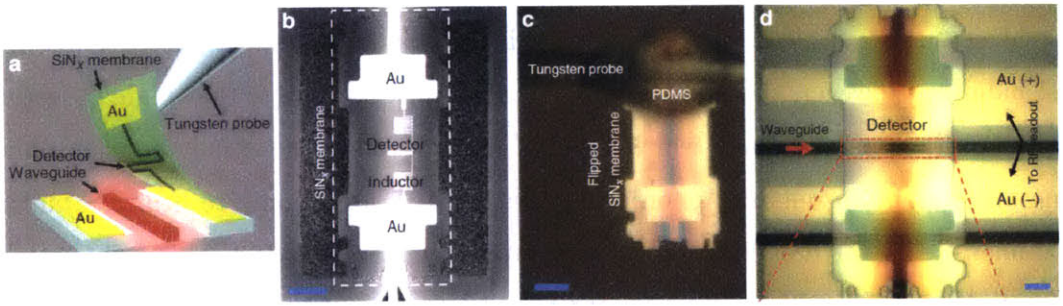

Figure 2-1: (a) Pick-and-place membrane transfer of an SNSPD onto a waveguide. (b) Suspended SNSPD membrane. (c) SNSPD membrane that was removed from the carrier chip using a tungsten microprobe with a drop of hardened PDMS at the tip. (d) SNSPD membrane integrated to a silicon waveguide [15].

We will integrate the bullseye membranes to a fiber by utilizing the pick-and-place membrane transfer method previously shown in our group by Najafi et al. [15]. Figure 2-1 is obtained from [15] to show how the pick-and-place method works. The important take-away is shown in Figure 2-1(b), which shows the design that results in sturdy bridges for holding the membrane in place after undercut but still brittle enough to easily break off with a tungsten microprobe during membrane transfer.

2.2.3 Modifications in Structure

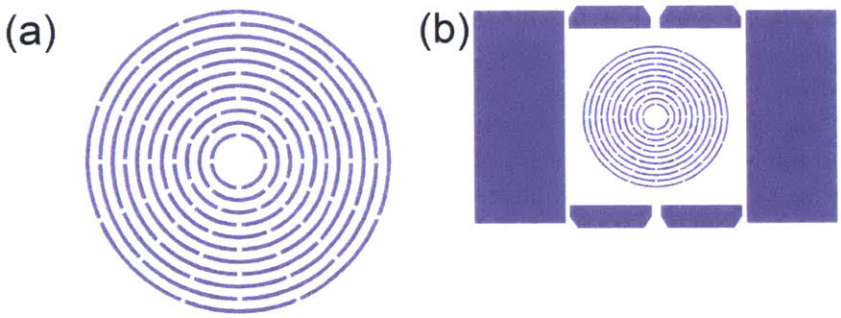

Figure 2-2: (a) Modification of bullseye structure for completely suspended structures. (b) Design for creating bullseye membranes that can be picked out.

As shown Figure 2-2(a), we have the modified design for the bullseye structure to be used for our purposes. Due to the nature of pick-and-place, the bottom surface of the membrane will be placed on top of the fiber facet. As such, we want fully etched trenches since it is currently not possible to correctly orient structures with partially etched trenches. As a result, this modified bullseye structure would have the same upward and downward emissions. In Figure 2-2(b), we have suspension bridges and large areas for undercut and prying that can be used to pick out the fully-suspended bullseye membranes. This provides an unpatterned surface area for the pick-and-place tungsten probe to adhere to without breaking the bullseye structure.

In order to show the result of modifying and optimizing the original bullseye structure, a commercial Finite-Difference Time-Domain (FDTD) solver software called Lumerical was used to compare the cavity mode and Purcell enhancement factor of each. From the results shown in Figure 2-3, we can see the behavior of the origi-

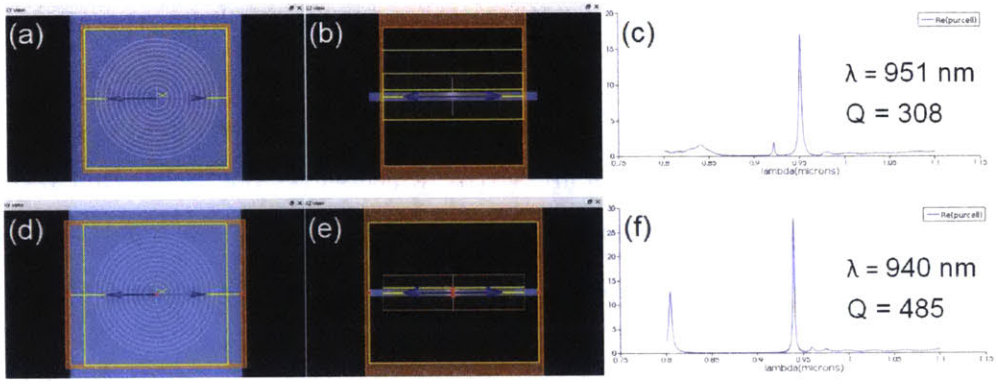

Figure 2-3: This is a comparison using the FDTD software Lumerical to see the difference between the original partial etch bullseye structure in Davanco et al. and the full etch modified bullseye structure we developed. For these simulations, the quantum dot dipole was assumed to be oriented along the xy plane, which means only the TE slab waves were excited. (a) and (b) show the simulation layout of partial etch bullseye structure, with a quantum dot dipole placed at the center of the structure. (c) Purcell enhancement spectrum associated with (a) and (b), which shows that the resonant wavelength is 951 nm and Q is 308. (d) and (e) show the simulation layout of the modified bullseye structure with suspension bridges to hold the structure when the trenches are fully etched, with a quantum dot dipole placed at the center of the structure. (f) Purcell enhancement spectrum associated with (d) and (e), which shows that the resonant wavelength is 940 nm and Q is 485.

nal bullseye cavity (top half) with that of the modified fully-etched bullseye cavity (bottom half). As shown, the fully etched trenches result in better field confinement, which results in higher cavity Q and higher Purcell factor. This means that this would potentially give a $g^{(2)}(0)$ that would be higher than zero due to the multiexcitonic and hybridized QD-wetting layer states being coupled to the cavity. Also, the full-etch design results in a blue-shift in the cavity mode.

Figure 2-4 shows the Lumerical simulation results of the complete system where the bullseye membrane is placed at the end of a fiber. The changes we had to make in the simulation compared to the design in Davanco et al. was that we have a different GaAs layer thickness (160 nm for our's vs. 190 nm for their's). As such, there is a difference in the TE mode effective index, which results in significant blue-shift. As a result, in order to maintain around the same resonant wavelength for the structure, we increased the grating period to compensate. Bridges were also incorporated in the bullseye structure in order to hold together the entire structure when the membrane

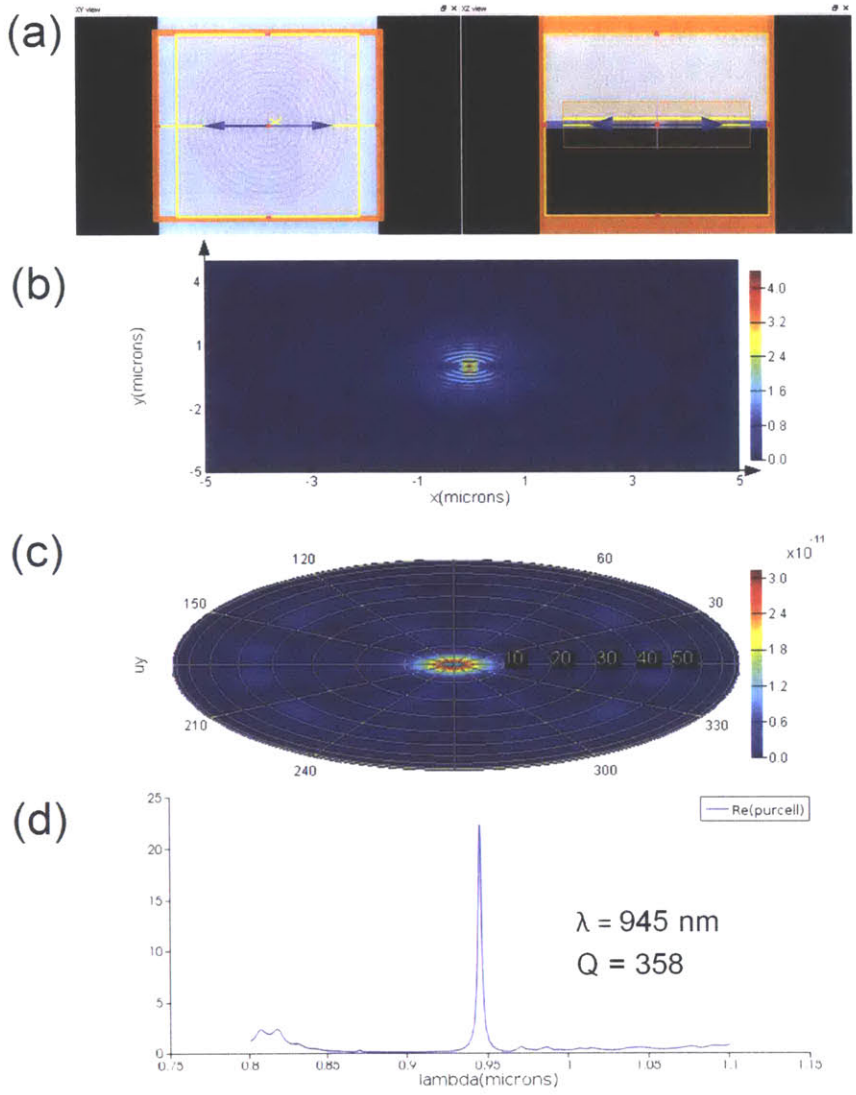

Figure 2-4: (a) and (b) show the simulation layout of the complete bullseye membrane on top of a fiber facet system. (b) Electric field intensity in the xy plane. (c) Far-field polar plot of the cavity mode. (d) Purcell enhancement spectrum, which shows that the resonant wavelength of the entire system is 945 nm and Q is 358.

is completely suspended. Also, a glass slab was included to represent the optical fiber. The structure was tuned and modified so that the xy electric field intensity and far-field polar plot remain the same, that way the emitted field remains nearly Gaussian and contained within 20° half-angle.

Figure 2-5 shows a comparison of our system with the original bullseye structure.

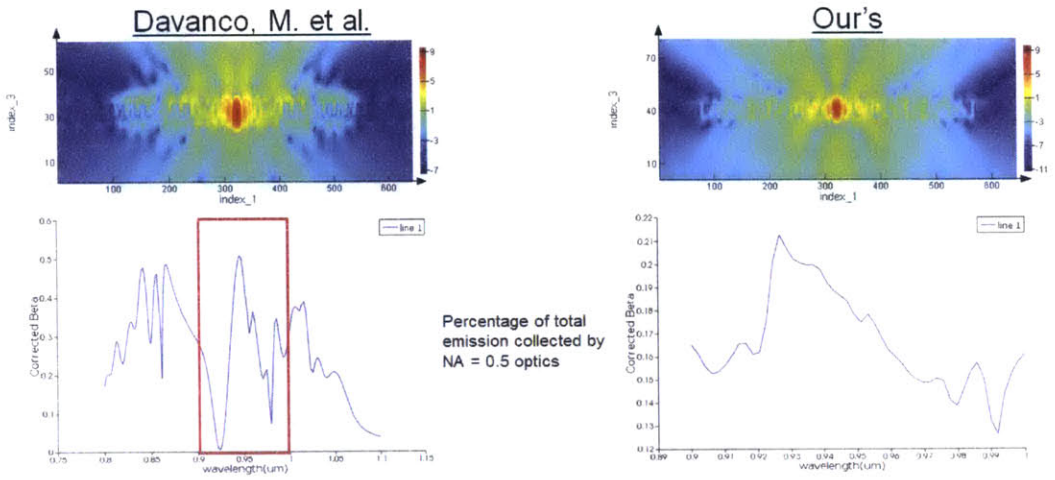

Figure 2-5: This is a comparison using the FDTD software Lumerical to see the difference between the original partial etch bullseye structure in Davanco et al. (left half) and the full etch modified bullseye structure we developed (right half). The top images are the log scale Electric field intensity of the circular grating structure in the xz plane. The bottom images show the percentage of total emission collected by NA = 0.5 optics as a function of wavelength.

We see that the percentage of total emission collected by NA = 0.5 optics for our system is about half compared to the original structure. However, we expect a higher experimental collection efficiency in practice due to direct coupling into fiber. That is because the paper involves free space optics, which typically has some loss.

2.3 Fabrication

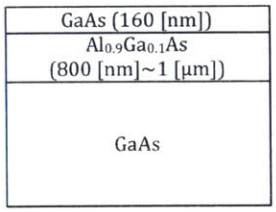

Figure 2-6: Starting substrate of the quantum dot wafers. The InAs quantum dots are embedded near the center of the GaAs layer.

Figure 2-6 shows the starting substrate of the quantum dot wafers. The InAs quantum dots are embedded near the center of the GaAs layer. Underneath the

GaAs layer is a sacrificial layer of $Al_{0.9}Ga_{0.1}As$, which can be undercut using HF to suspend the structures in the top 160nm GaAs layer. Finally, all of this is on top of a GaAs substrate. All the fabrication was done using the Technology Research Laboratory cleanroom, which is part of MIT's Microsystems Technology Laboratories. The fabrication process is the following:

1. Clean small 5 mm by 5 mm unpatterned chips with sonication in acetone, methanol, and isopropyl alcohol, consecutively, for 5 minutes each.

2. Spin coat ZEP520A electron beam resist at 4000 rpm for 2 minute, then bake at 180°C for 3 minute. This results in about 350 nm of ZEP520A film as resist mask. ZEP520A is used since it has good resolution and high contrast, faster write time than PMMA since it has a lower dose to clear, and better etch resistance than PMMA.

3. Spin Espacer at 4000 rpm for 1 minute. This is to help with the conductivity of the sample during the electron beam lithography write to prevent charging.

4. Use the Elionix ebeam writer to pattern the resist, using about 320 $\mu C/cm^2$ dose to clear.

5. Immerse in DI water for 1 minute to remove Espacer.

6. Develop in o-Xylene for 2 minute 30 seconds, followed by a 30 second rinse in IPA to stop development.

7. Dry etch through the 160 nm GaAs layer using SAMCO ICP-RIE, using a $Cl_2/SiCl_4/Ar$ dry etch chemistry.

8. Immerse the sample in 1% HF for 1 minute 30 seconds. This undercuts the $Al_{0.9}Ga_{0.1}As$ sacrificial layer in order to suspend the bullseye structures.

9. Remove the ZEP520A by immersing in 85°C NMP for 2 hours. Oxygen plasma clean is avoided in order to not damage the quality of the top GaAs surface.

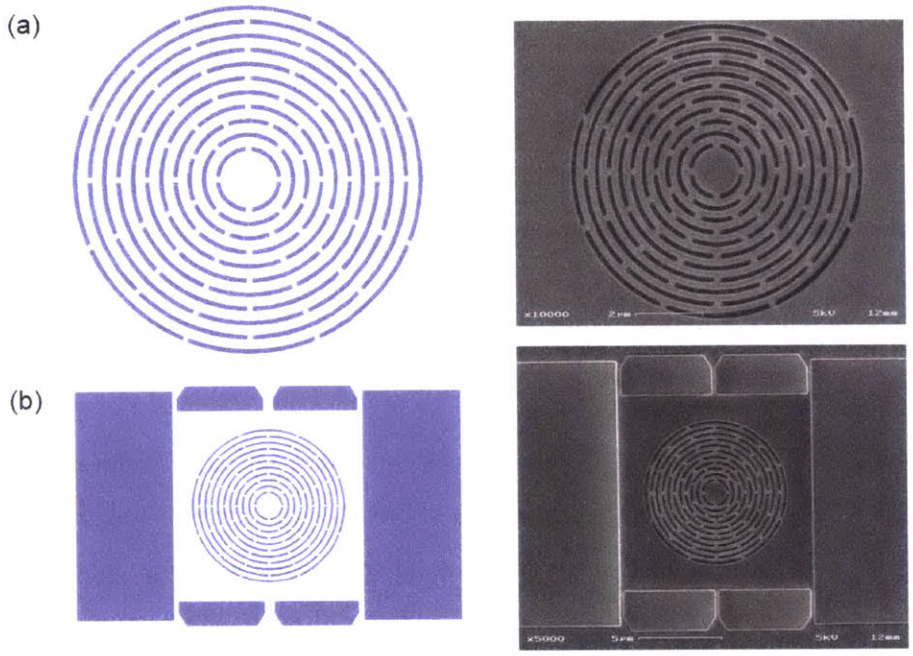

Figure 2-7: (a) Left: design, right: fabricated structures of "bullseye" circular grating (b) Left: design, right: fabricated structures of "bullseye" circular grating with suspended bridges that can be broken to systematically place the structure on a fiber facet.

Figure 2-7 shows the result of the fabrication (at least from a top-down view using a SEM) of the QD circular grating structure. The fabricated structures look very good, no residual resist or other debris.

2.4 Experimental Results

2.4.1 Optical Setup

For the experimental setup, an excitation laser at 852 nm is used. Collinear to the path is a collimated white light source to illuminate the sample. The laser is reflected off a two mirror galvos and into a 4F imaging system (the principle of the 4F imaging is shown in Figure 2-8), followed by a 50x NIR microscope objective and onto the sample. A galvos and 4F imaging system is used for confocal imaging since there is no translational piezo stage for the sample in the cryostat. The galvos and 4F result

in an effective translation of the sample during imaging without actually moving the sample. The 4F is two lenses placed at a sum of the focal distance of each of the two lenses away from each other. Then, one lens is placed at a focal distance away from the galvos, the other is placed at a focal distance away from the aperture of the microscope objective. The galvos will give an angle to the laser entering the 4F. The 4F will do a correction such that the beam entering the objective will have that angle without the translation with respect to the central axis.

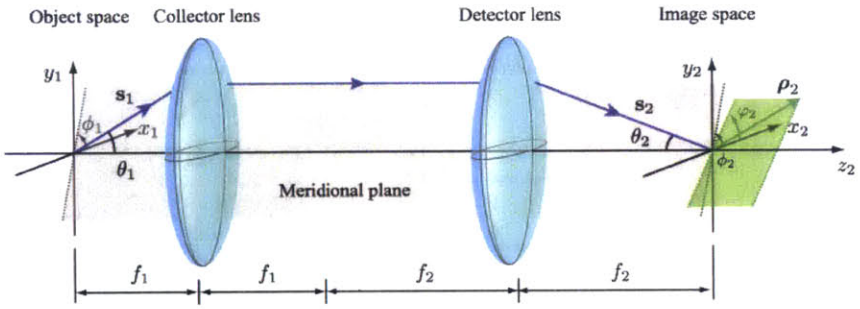

Figure 2-8: 4F imaging configuration [10].

The emission and image of the quantum dots then goes through the objective, 4F, and galvos. Afterwards, it goes into either a CCD camera, out-couples into a fiber to a spectrometer, out-couples into a fiber to an APD counter, or into a free-space spectrometer. When the emission is out-coupled into a fiber to the spectrometer or APD, the fiber acts as a spatial filter to get the same effect as confocal imaging optics. On the other hand, when the emission is sent into a free-space spectrometer, an actual confocal imaging system is used. Figure 2-9 is the experimental setup used for characterizing the quantum dot chips. A portion of the microscope setup is on top of an elevated optical platform so that the objective can be suspended over the Montana closed-cycle cryostat, as shown in Figure 2-10. All the beam paths are aligned to travel parallel with the holes in the optical table. This is necessary for the X and Y translational stages that we will discuss further: Part of the optics on top of the elevated optical table are on top of a Y translational stage that travels parallel to the beam path in order to roughly translate the optics along the Y axis with respect to the sample in the cryostat. Part of the optics on top of the Y translational stage

are on top of a X translational stage that travels parallel to the beam path in order to roughly translate the optics along the X axis with respect to the sample in the cryostat. Right before the free-space spectrometer, there is a lens that focuses the collimated beam to a pinhole, followed by another lens to collimated the beam; this is the confocal imaging optics.

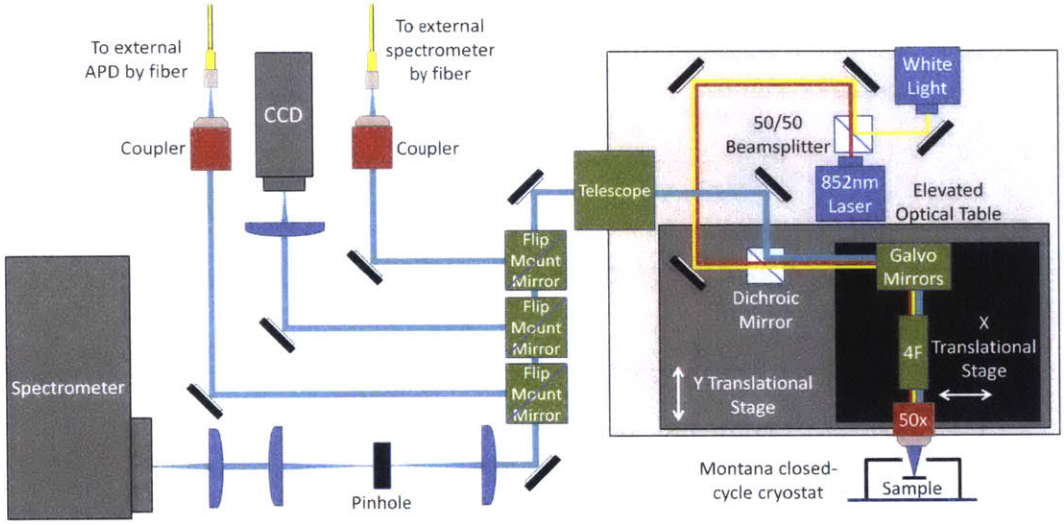

Figure 2-9: Experimental setup for quantum dot experiments.

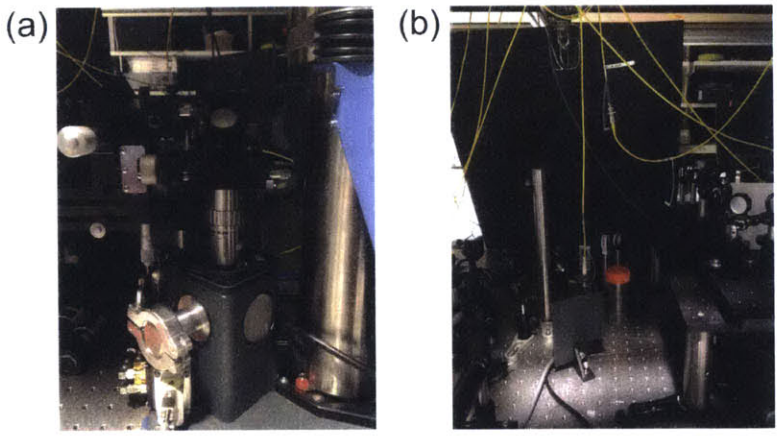

Figure 2-10: (a) Microscope objective directly over Montana cryostat. (b) Portion of setup that transitions from the elevated optical platform to the optical table.

2.4.2 Spectroscopy Experiments

For the experiments to be described, the free space spectrometer was used for all spectrum measurements, and the external APD was used for doing the confocal scanning. For the spectroscopy experiments, we first do a confocal scan zoomed out to the largest field of view possible in order to see which bullseye has an enhanced fluorescence at its center. Since there should be a Purcell enhancement of about 20, we would expect good structures to have a much brighter spot than the surrounding unpatterned bulk QD regions. This is exactly what we see in Figure 2-11(a), where all the bright spots coincide with the location of the bullseyes. After we know the general proximity of each bullseye, we can zoom in to each individual bullseye by modifying the scan area and increasing the resolution. This is done by finely controlling the voltage applied to each galvos mirror, which finely tunes the galvos mirror positions. Figure 2-11(b) is a zoomed-in confocal scan of the fluorescence of a single bullseye circular grating. We can see clearly that there is a significantly much brighter spot at the center of the structure.

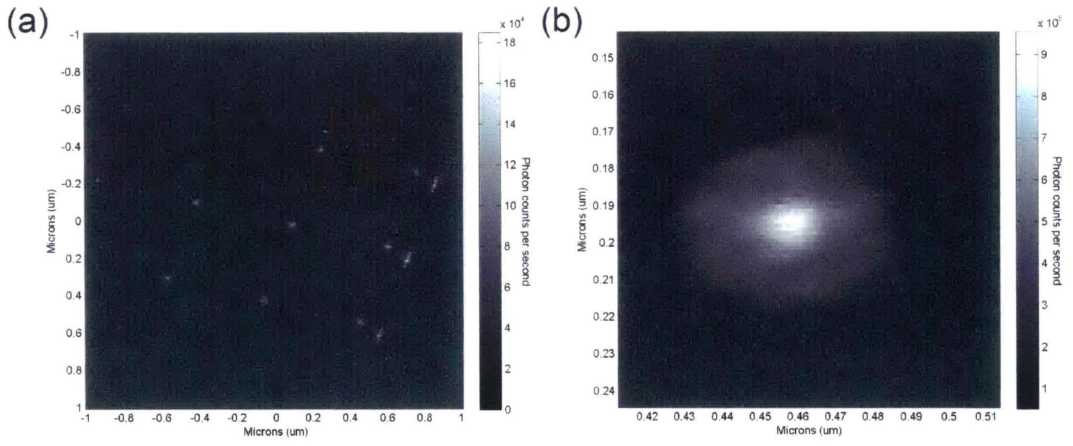

Figure 2-11: (a) Confocal scan of the fluorescence of an array of bullseye circular gratings. (b) Zoomed-in confocal scan of the fluorescence of one bullseye circular grating. Note: the dimensions on the side are not the actual physical dimensions of the scan, but rather the voltage applied to each galvos mirror.

Then, we can park the galvos mirrors such that the beam spot from the objective (and the collection spot) is at the center of the bright fluorescence. Next, we flip

the flip-mount mirrors such that the collection path goes into the confocal imaging optics and into the spectrometer to take the spectrum. Figure 2-13 is an example of a bullseye circular grating spectrum while Figure 2-12 shows the spectrum of the bulk quantum dots for comparison. We see a significant resonance peak at around 935nm, which is just 5nm off from the simulated spectrum shown in Figure 2-3(f). This is reasonable considering slight fabrication imperfections. It looks like the peak width is about 5nm, as simulated. However, this is not easy to see because the spectrum has some of the bulk QD characteristics added to the resonance peak. This is probably due to the excitation beam and collection spot size being bigger than the bullseye structure. This can be fixed either by using a higher NA objective or reducing the pinhole size in the confocal imaging optics.

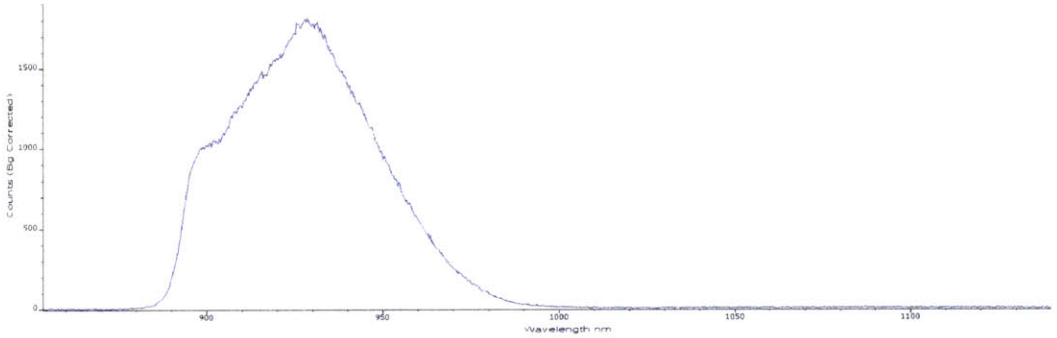

Figure 2-12: Spectrum of the bulk quantum dots at an unpatterned area.

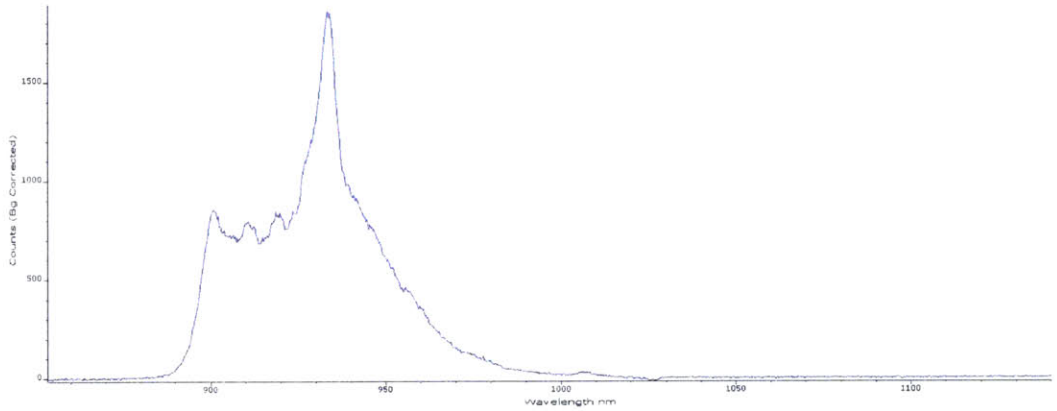

Figure 2-13: Spectrum at the center of a bullseye structure with a bright enhanced fluorescence spot.

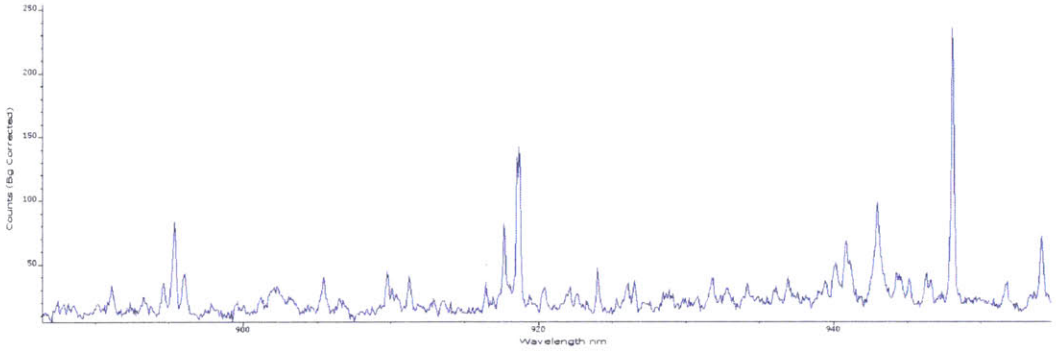

Figure 2-14: Spectrum at the center of a bullseye structure with a bright enhanced fluorescence spot, using a higher density grating and lower pump power.

The next step for characterizing the bullseye structures would be to use a higher density grating in the spectrometer in order to get a higher resolution spectrum. Using this grating, the pump power is decreased until single exciton lines like the ones shown in Figure 2-14 can be seen. At sufficiently low pump power, we should be able to see a single exciton line that gets dramatically enhanced when the respective QD overlaps with a cavity both spatially and spectrally. However, that is something we have not been able to observe. Usually to get a QD that overlaps with the cavity perfectly spatially, we would need to tune the QD emission wavelength by tuning the temperature. Nonetheless, this did not seem to work, and it did not appear as if the QD emission spectrum was changing when the cryostat temperature was tuned. A potential explanation for this is that perhaps the sample was not making a good thermal contact with the cryostat cold head, so it was not actually at the temperature we desired it to be. This is something to be sorted out in the near future.

Once we can determine from spectroscopy experiments that we have a QD that is aligned perfectly spatially and spectrally to a bullseye, then the emission can be sent to a Hanbury Brown-Twiss interferometer that uses APDs for detection to measure the photon autocorrelation statistics to check the single-photon characteristics of that QD. Once a good QD in a good bullseye structure is found, then we would pick-and-place the bullseye membrane onto a fiber facet and repeat the same experiments while expecting higher collection efficiency. This can also be extended to Li et al.'s previous work in which they demonstrated record-high photon collection rate from a single NV

center by using bullseye circular gratings [12]. By integrating the bullseye structure with an NV in it to the facet of a high NA fiber, we can expect to get an even higher photon collection rate.

Chapter 3

Quantum Repeater using NV and Wide-Bandgap Programmable Nanophotonic Processor

3.1 Overview and Vision

For this portion of the thesis, I will highlight our efforts to create a quantum repeater for long-distance quantum communication and distributed quantum computing. For this, we will be using nitrogen vacancy centers in diamond as quantum memories. We also need to be able to generate entanglement between two quantum memories on-chip by entangling the photons that are entangled with each quantum memory. To do so, we would need a wide-bandgap programmable nanophotonic processor (or circuit) that is capable of entangling visible wavelength photons between two quantum memories on chip via a 50:50 splitter and detection via superconducting nanowire single-photon detectors (SNSPDs) at the output arms. As we have in our arsenal the pick-and-place membrane transfer method, we can use different material systems for this method by fabricating the different components separately and transferring them to the host device with the programmable nanophotonic processor. As such, we require the host device material to be a wide bandgap semiconductor, with high

thermal conductivity and small thermo-optic coefficient so that the entire system can be placed in a cryostat and remain operational since the SNSPDs operate at cryogenic temperatures. In addition, we require the host device material to have electro-optic tuning capabilities in order to tune on-chip filters and phase shifters. Figure 3-1 is an overview of the quantum repeater hardware that we propose. The AlN dynamic photonic routing circuit is an optical mesh of cascaded tunable Mach-Zehnder interferometers with phase shifters for accurately tuning the output splitting. These phase shifters are necessary since it is typically impossible to make directional couplers with exact 50:50 splitting ratios, so the phase shifters help compensate for these fabrication imperfections. In addition, the programmable nanophotonic processors can be programmed to implement any arbitrary unitary optical transformations.

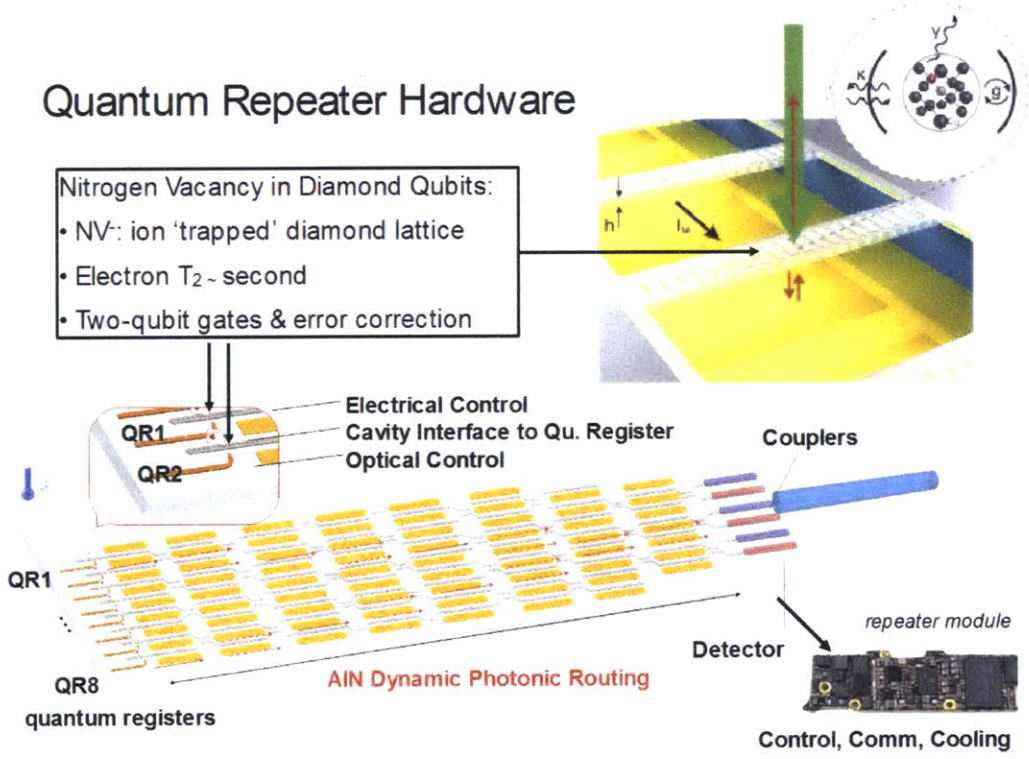

Figure 3-1: Overview of quantum repeater hardware, which uses nitrogen vacancy centers in diamond as quantum registers, AlN photonic integrated circuit for dynamic photonic routing, and SNSPDs as on-chip detectors.

3.2 Aluminum Nitride

For our host device material, we decided to use aluminum nitride since it has a large bandgap of 6.2 eV, high thermal conductivity of κ_{AlN} = 285 W/m·K, small thermo-optic coefficient of $dn_{AlN}/dT = 2.32 \times 10^{-5}$/K, a fairly good electro-optic coefficient of r_{32}, $r_{13} \sim 1$ pm/V, and an added bonus of $\chi^{(2)}$ of about 4.7 pm/V. The large bandgap means that AlN can operate in the ultraviolet, visible, and mid-infrared. Its high thermal conductivity and small thermo-optic coefficients mean that we can operate the entire device at cryogenic temperatures without the optical and physical properties of the AlN changing too much. The electro-optic coefficient is useful for tuning the optical properties of the AlN by applying an electric field across it. Finally, even though its $\chi^{(2)}$ is no match for lithium niobate's $\chi^{(2)}$ of 16 pm/V, AlN is an easier material to process and fabricate compared to lithium niobate. The $\chi^{(2)}$ allows for frequency doubling, parametric frequency conversion, sum/difference frequency generation, electro-optic modulators, optical parametric oscillators, frequency combs, and much more. Frequency conversion is especially useful for interfacing the NV quantum memories with telecom photons that are usually used as flying qubits for long distance communication.

To scalably create many of these AlN programmable nanophotonic processor devices sometime in the future, we would need an AlN foundry process similar to the one for silicon photonics of today, where there are multi-project runs that help distribute fabrication costs amongst a larger number of end-users. One of the long term goals, which I have started doing for this Master's Thesis, is to work with Sandia National Laboratories to develop a large-scale AlN fabrication process.

Chapter 4

Passive Components of Aluminum Nitride Photonic Integrated Circuit

4.1 Adiabatic Waveguide Taper

The diamond nanobeam cavity membranes with an implanted nitrogen vacancy center in the center will be pick-and-placed onto the AlN photonic integrated circuit at a waveguide taper region that adiabatically transitions between the diamond membrane's waveguide mode and the AlN waveguide's mode. This design is taken exactly from a previous publication in my group by Mouradian et al. in 2014 [14], with a pertinent figure shown in Figure 4-1. The optimal device geometry was found by calculating the coupling efficiency from the fundamental TE mode of the diamond microwaveguide and the SiN waveguide while sweeping both the diamond microwaveguide and SiN waveguide taper lengths. Since SiN and AlN have very similar refractive indices at 637 nm (2.01 versus 2.15, respectively), we can expect the same waveguide taper in SiN to behave closely when applied to AlN.

The paper showed that a 2 μm gap in the SiN waveguide, a SiN waveguide taper length of 5 μm, and a diamond microwaveguide taper length of 6 μm would result in a coupling efficiency of 41.5% coupled to each side of the SiN waveguide separated by the gap (or 83% total into the SiN waveguide).

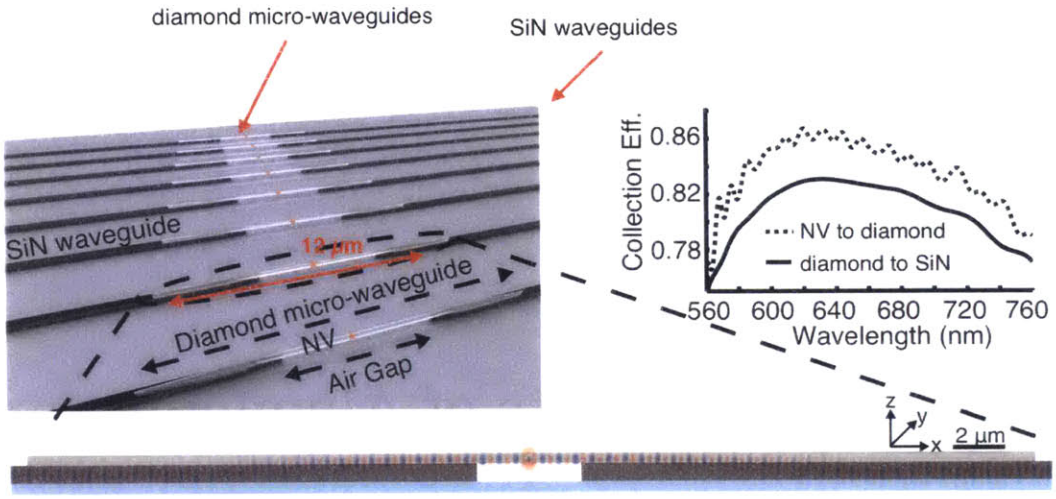

Figure 4-1: Adiabatic waveguide taper for coupling light efficiently from diamond nanobeam cavities to AlN waveguide. This design is taken exactly as-is from Mouradian et al.'s 2014 paper [14].

4.2 Bragg Grating Filter

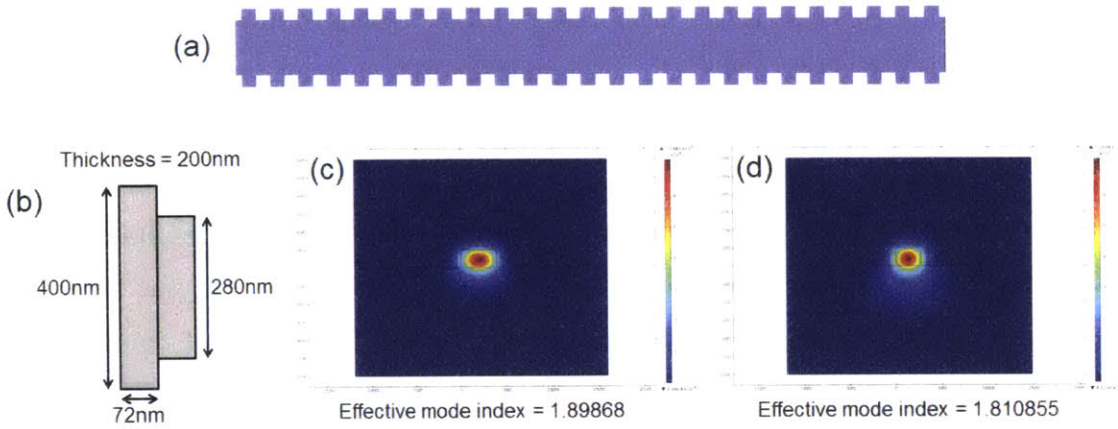

Figure 4-2: (a) Overall design of Bragg Grating filter, which is used for filtering the 532 nm green excitation laser and allowing the 637 nm NV fluorescence to pass through. (b) Dimensions of the Bragg Grating filter, where the period is 144 nm, the original waveguide width is 400 nm, the corrugated waveguide width is 280 nm, and the thickness of the waveguide is 200 nm. (c) Electric field profile of the larger width 400 nm cross section, which has an effective mode index of 1.89868. (d) Electric field profile of the smaller width 280 nm corrugated cross section, which has an effective mode index of 1.810855.

As shown in Figure 4-2, this is the design and Lumerical MODE Solutions simu-

lation results of the waveguide Bragg Grating filter. Figure 4-2(a) shows the overall design and what it looks like when the Bragg Grating filter is repeated for 25 periods. Simply put, the design is a strip of waveguide with periodic sidewall corrugations, which results in a periodic modulation of the effective refractive index of the optical mode. At each corrugation boundary, part of the travelling light is reflected, where the relative phase of the reflected light is a function of the grating period and the light wavelength. As such, a Bragg Grating can be thought of as a 1D photonic crystal, so the filtering property is a result of the photonic bandgap that is formed in this structure. The repeated corrugation in the wavelength causes multiple and distributed reflections, and the reflected light interferes constructively in a narrow band around the Bragg wavelength. Outside this wavelength band, the multiple reflections interfere destructively and result in the light being transmitted through the grating. Figure 4-2(b) shows the exact dimensions of the Bragg Grating filter, where the period is 144 nm, the original waveguide width is 400 nm, the corrugated waveguide width is 280 nm, and the thickness of the waveguide is 200 nm. The rough design was done by finding the n_{eff} of the region with the larger waveguide width of 400 nm and the n_{eff} for the smaller waveguide width of 280 nm, followed by using the Bragg condition:

$$\begin{aligned} \lambda_0 &= 2n_{eff}\Lambda \\ \Lambda &= \frac{\lambda}{2n_{eff}} \end{aligned} \tag{4.1}$$

where λ_0 is the wavelength of the green excitation laser we want to reflect and filter, which is 532nm. n_{eff} is the effective refractive index of the complete Bragg Grating filter, which we take to be approximately equal to the average of the effective mode index of the wider and thinner cross sections of the filter. Finally, Λ is the grating period. The transmission and reflection spectra of a Bragg Grating can be calculated analytically using Coupled Mode Theory, which says that the reflection coefficient for a grating of length L is [4]:

$$r = \frac{-i\kappa \sinh(\gamma L)}{\gamma \cosh(\gamma L) + i\Delta\beta \sinh(\gamma L)} \tag{4.2}$$

where $\gamma^2 = \kappa^2 - \Delta\beta^2$. κ is the coupling coefficient of the grating, or the amount of reflection per unit length. $\Delta\beta$ is the propagation constant when offset from the Bragg wavelength, where $\Delta\beta = \beta - \beta_0 \ll \beta_0$. If we want to get the peak power reflectivity at the Bragg wavelength where $r = -i\tanh(\kappa L)$, then we use:

$$R_{peak} = \tanh^2(\kappa L) \tag{4.3}$$

The bandwidth of the Bragg Grating filter can then be calculated by using:

$$\Delta\gamma = \frac{\gamma_B^2}{\pi n_g}\sqrt{\kappa^2 + \left(\frac{\pi}{L}\right)^2} \tag{4.4}$$

where n_g is the group index. When the Bragg Grating is many periods long, which means that $\kappa \gg \frac{\pi}{L}$, then we get that the bandwidth of the Bragg Grating filter becomes:

$$\Delta\gamma = \frac{\gamma_B^2 \kappa}{\pi n_g} \tag{4.5}$$

Hence, from the equation of the Bragg Grating filter peak power reflectivity at the Bragg wavelength and the equation for the bandwidth, we know that higher corrugation width results in an increased coupling coefficient κ, which results in a higher reflectivity and broader bandwidth. This is what we considered in designing the Bragg Grating filter for filtering out the excitation pump.

Figure 4-3(a) shows the Lumerical FDTD simulation results of the Bragg Grating filter, which was set to find the bandstructure spectrum at the band edge of $k_x = \pi/a$. The two peaks give the location and span of the band gap. Although this simulation was done for an infinitely long periodic Bragg Grating with infinite periods, it serves as a good approximation for how the Bragg Grating would behave when we do have a

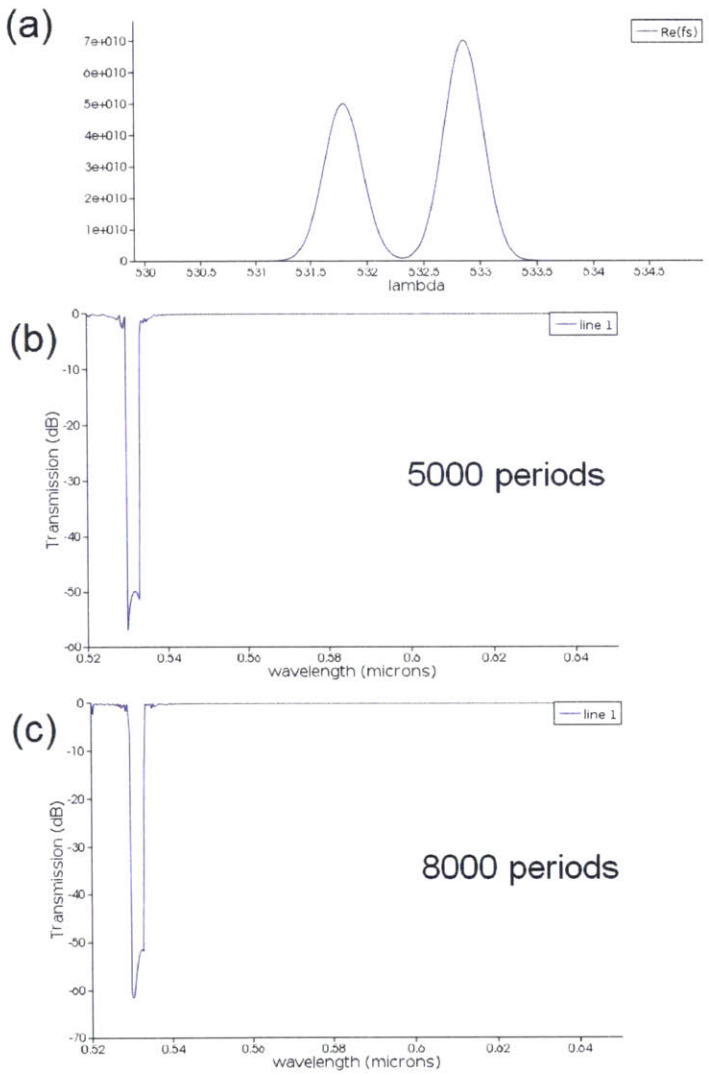

Figure 4-3: (a) Bandstructure spectrum at the band edge $k_x = \pi/a$. (b) Transmission spectrum for 5000 periods. (c) Transmission spectrum for 8000 periods.

sufficiently large number of periods. We can see from the images that the two peaks are at around 531.8 nm and 532.8 nm, which means that the band gap covers the wavelength of 532 nm of the excitation laser that we want to filter out. Figure 4-3(b) shows the Lumerical MODE Solutions simulation result for calculating the full transmission spectrum given that the Bragg Grating filter is 5000 periods long. We see that there is a dip for wavelengths between 529.7 nm and 532.8 nm and an extinction ratio of about 58 db. Figure 4-3(b) shows the Lumerical MODE Solutions simulation

result for calculating the full transmission spectrum given that the Bragg Grating filter is 8000 periods long. We see that there is a dip for wavelengths between 529.7 nm and 532.8 nm and an extinction ratio of about 61 db. In addition, Figure 4-3(b), (c) show that there should be 100% transmission for 637 nm, which is the fluorescence wavelength of the Nitrogen Vacancy center.

4.3 Disk Resonator

Nitrogen Vancancy centers in diamond suffer from a phenomenon called spectral diffusion in which there are random jumps in the emission wavelength of the zero phonon line. Several GHz wide spectral diffusion is typically an issue for implanted NVs near the surface when pumped off-resonantly, which leads the zero phonon line to broaden. This causes the photons emitted from the NV to no longer be indistinguishable [25]. In order to combat this and to entangle two indistinguishable photons from two different NV quantum memories, we will utilize disk resonators that can be tuned electrically using AlN's piezoelectric properties.

4.3.1 Dependence on Coupling Gap

Figures 4-4, 4-5, and 4-6, highlight the dependence of the coupling gap and getting critical coupling between the microdisk and the bus waveguides. For these designs, we have two things to consider: 1. the microdisk has to be at least 30 μm in radius since they need to be sufficiently large enough for electrical contacts to control the piezoelectric properties and 2. the microdisk is expected to have a Q of around 10,000 since this is what was measured to be experimentally achievable by Sandia National Laboratories' AlN fabrication efforts previously. We obtain a Q of around 10,000 in the simulation microdisks by introducing a value in the imaginary portion of the material refractive index to mimic loss in the material. Since we are expecting the disk to have Q of 10,000, it was challenging to find the right coupling mechanism to get critical coupling. Obviously a single point coupling scheme would not be sufficient to load a disk with such high loss, so a wrap-around scheme has to be used. For

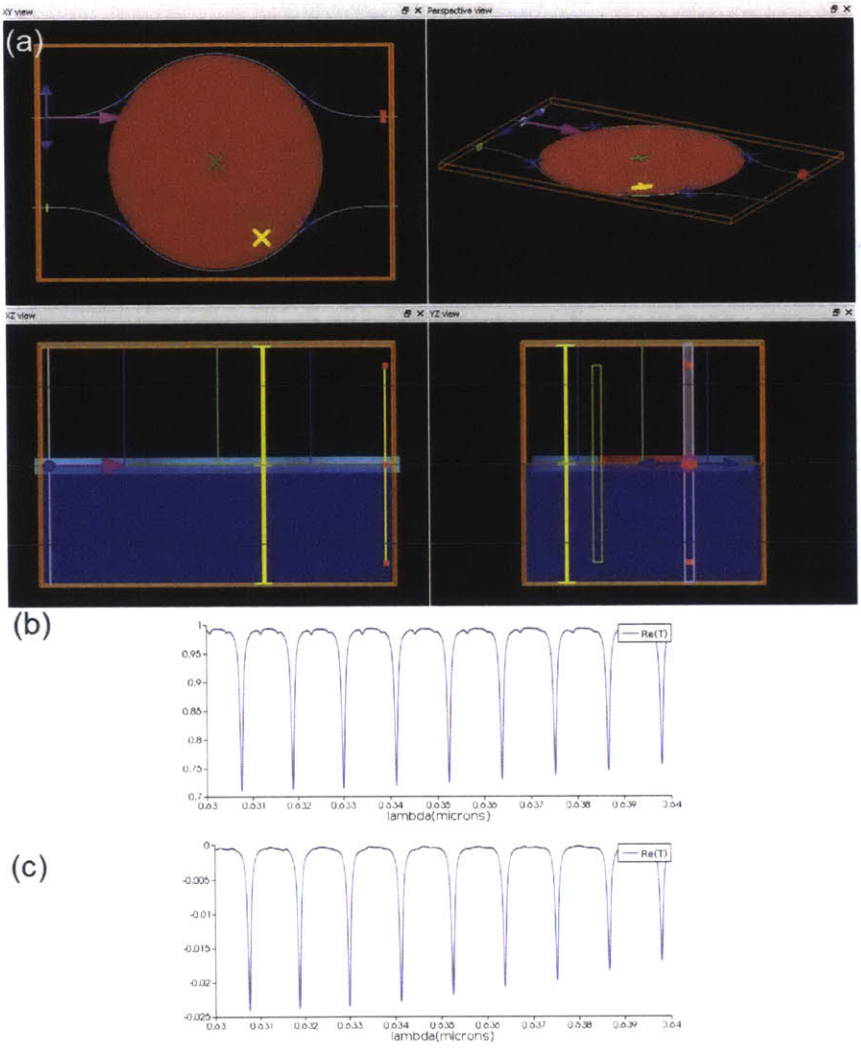

Figure 4-4: (a) Simulation setup for a disk resonator of 30 μm coupled to two bus waveguides by a coupling length of 12.3890 μm and coupling gap of 200 nm. The input port is at the top left, the through port is at the top right, and the drop port is at the bottom left. (b) Transmission spectrum of the through port. (c) Transmission spectrum of the drop port.

these designs, we have two bus waveguides coupling to the microdisk, that way we can either use the through port or the drop port for filtering. From 4-4(b), 4-5(b), and 4-6(b), we see that we get closer and closer to critical coupling as we decrease the coupling gap. However, we never actually get to critical coupling since we do not get dips in the through port transmission spectrum that reach sufficiently close to 0. Though we do for a coupling gap of 50 nm, the off-resonance transmission is

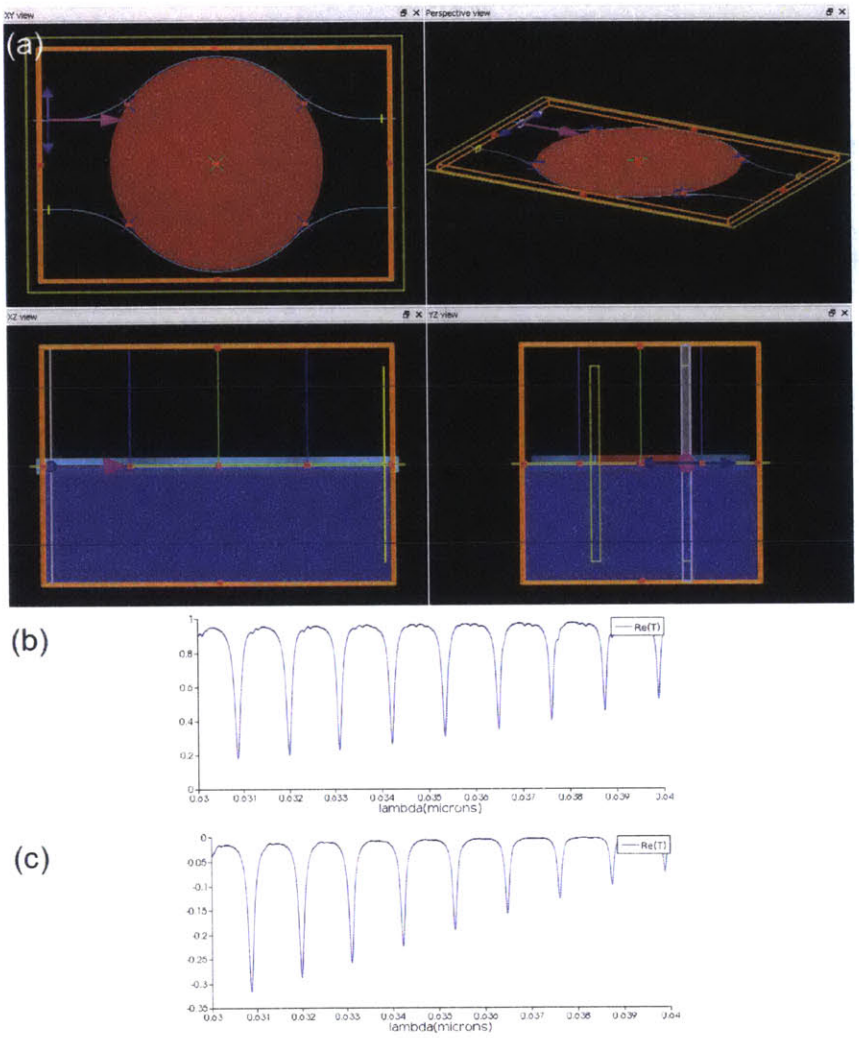

Figure 4-5: (a) Simulation setup for a disk resonator of 30 μm coupled to two bus waveguides by a coupling length of 12.3890 μm and coupling gap of 100 nm. The input port is at the top left, the through port is at the top right, and the drop port is at the bottom left. (b) Transmission spectrum of the through port. (c) Transmission spectrum of the drop port.

not 1 either, meaning we do not have critical coupling. A coupling gap of 50 nm is the minimum we are willing to consider since beyond that, the structures would be difficult to fabricate, even with electron beam lithography. Ideally, we would use a gap of 200 nm since that is the limit of optical lithography and something easily achievable by electron beam lithography.

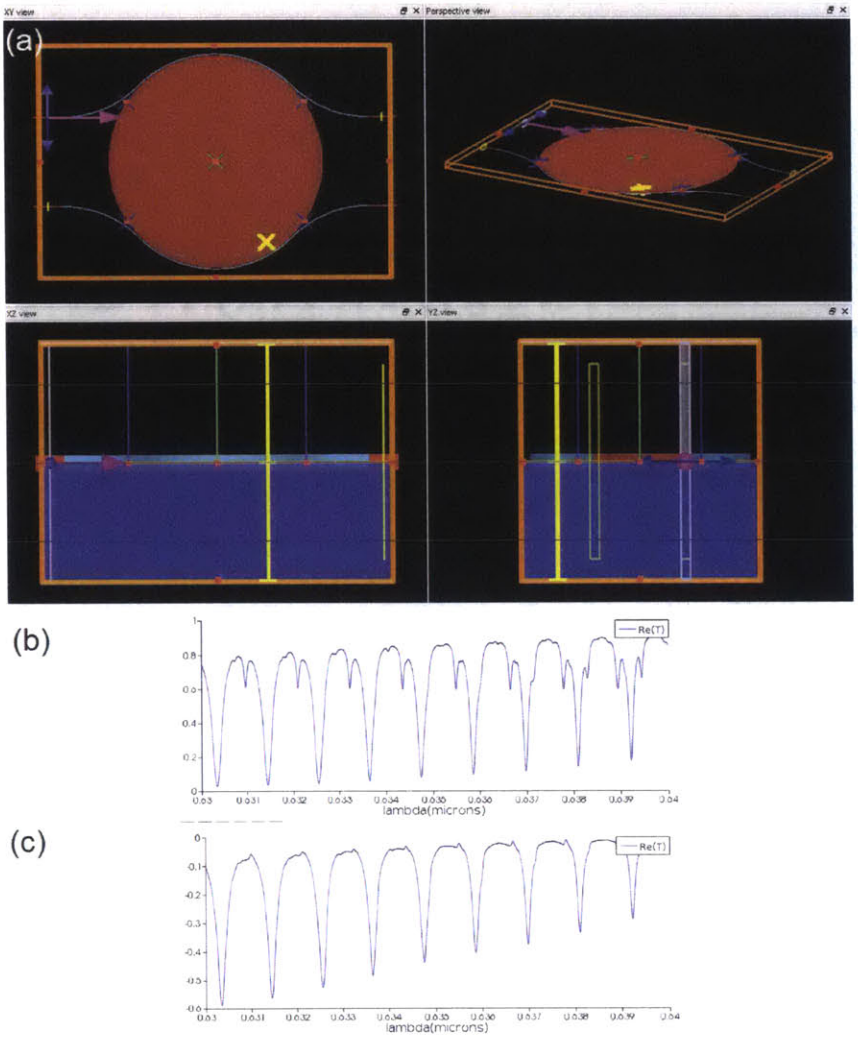

Figure 4-6: (a) Simulation setup for a disk resonator of 30 μm coupled to two bus waveguides by a coupling length of 12.3890 μm and coupling gap of 50 nm. The input port is at the top left, the through port is at the top right, and the drop port is at the bottom left. (b) Transmission spectrum of the through port. (c) Transmission spectrum of the drop port .

4.3.2 Dependence on Coupling Length

Figures 4-7, 4-8, and 4-9, highlight the dependence of the coupling length and getting critical coupling between the microdisk and the bus waveguides. The results from Figures 4-7 is meant to be compared with those from Figure 4-6 since the coupling gap is kept the same at 50 nm but the coupling length is changed to 60 μm from 47.124 μm. In this comparison, we see that the on-resonance transmission dips remain sufficiently

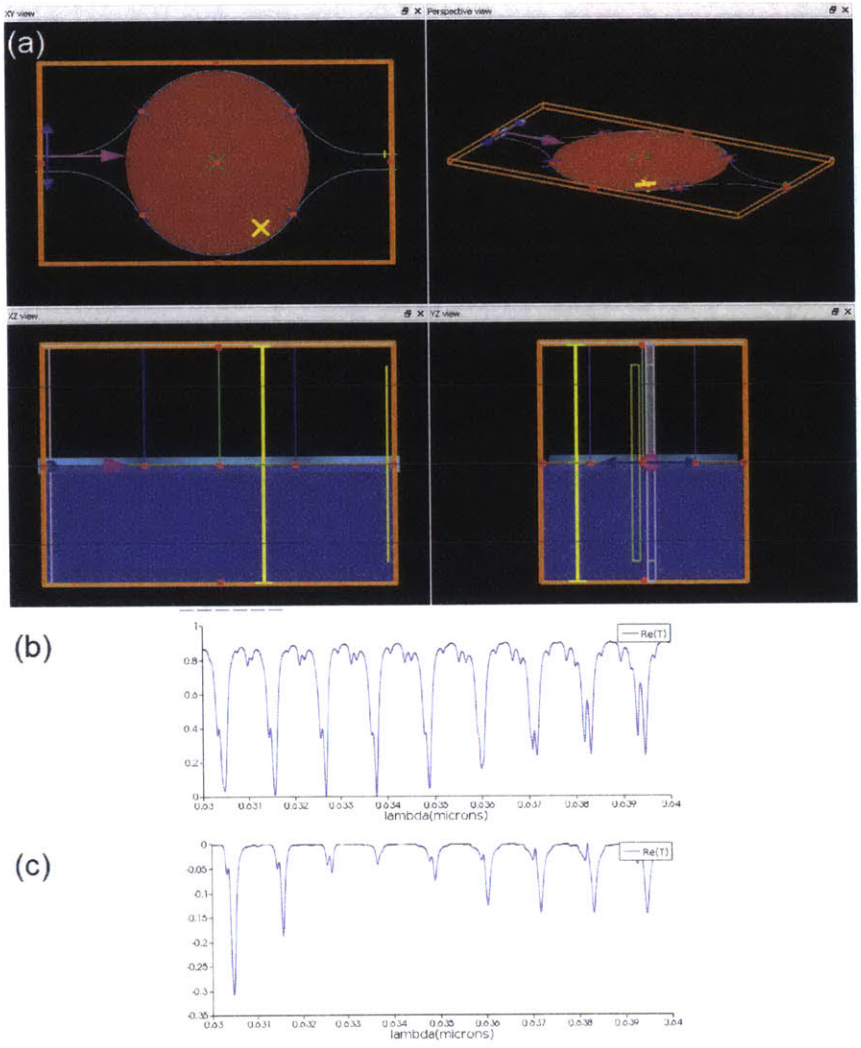

Figure 4-7: (a) Simulation setup for a disk resonator of 30 μm coupled to two bus waveguides by a coupling length of 60 μm and coupling gap of 50 nm. The input port is at the top left, the through port is at the top right, and the drop port is at the bottom left. (b) Transmission spectrum of the through port. (c) Transmission spectrum of the drop port.

close to 0 as the coupling length is increased. The difference is that the off-resonance transmission becomes closer to 1 as the coupling length is increased, which means we approach critical coupling. However, a coupling length of 60 μm is near the limit for a microdisk with radius 30 μm without the two bus waveguides intersecting with each other. As such, to get critical coupling to the microdisk, we also considered using only one bus waveguide and using the through port for filtering, rather than having the

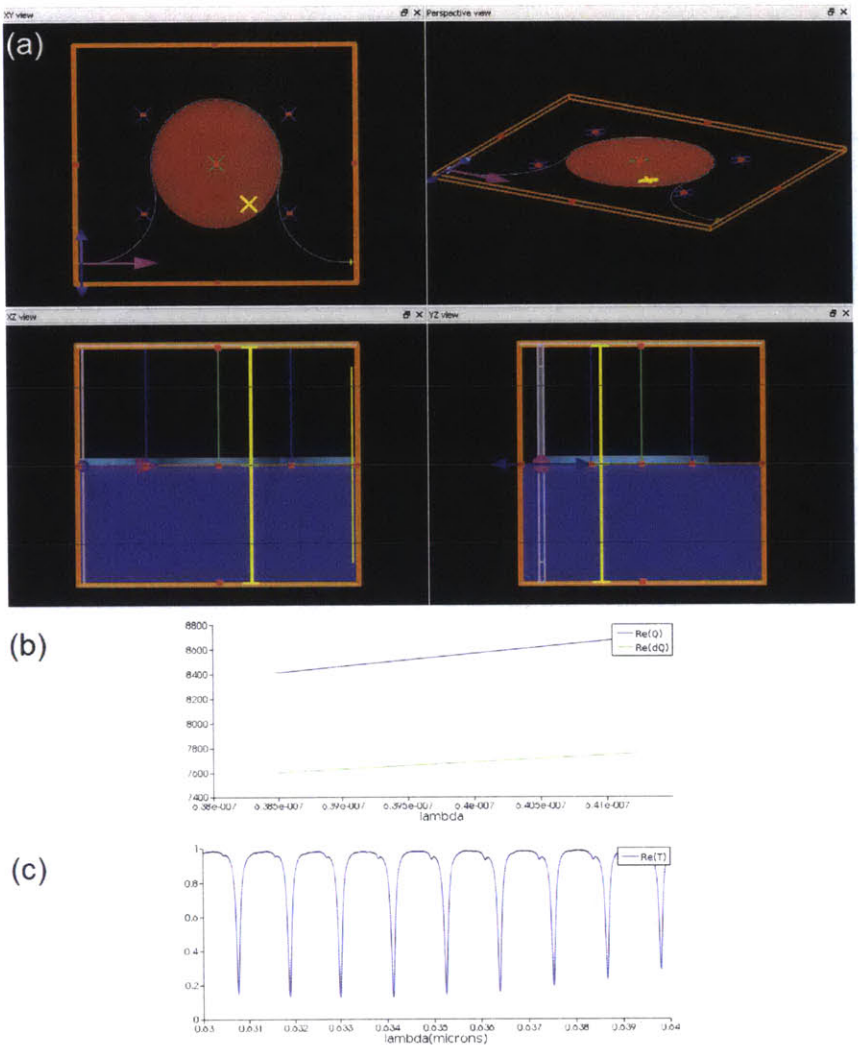

Figure 4-8: (a) Simulation setup for a disk resonator of 30 μm coupled to one bus waveguide by a coupling length of 100 μm and coupling gap of 200 nm. The input port is at the bottom left and the through port is at the bottom right. (b) Spectrum of the Q factor of the disk as a function of wavelength. (c) Transmission spectrum of the through port.

option of using either the through port or drop port for filtering. Figures 4-8 and 4-9 show these results. Comparing these results with Figure 4-4 since these simulations all have the same coupling gap of 200 nm but different coupling lengths, we see that we do approach critical coupling as we increase the coupling length. Finally, we reach critical coupling in Figure 4-9, where the coupling length is 150 μm. Figure 4-9(c) shows that the off-resonance transmission is 1 while the on-resonance transmission is

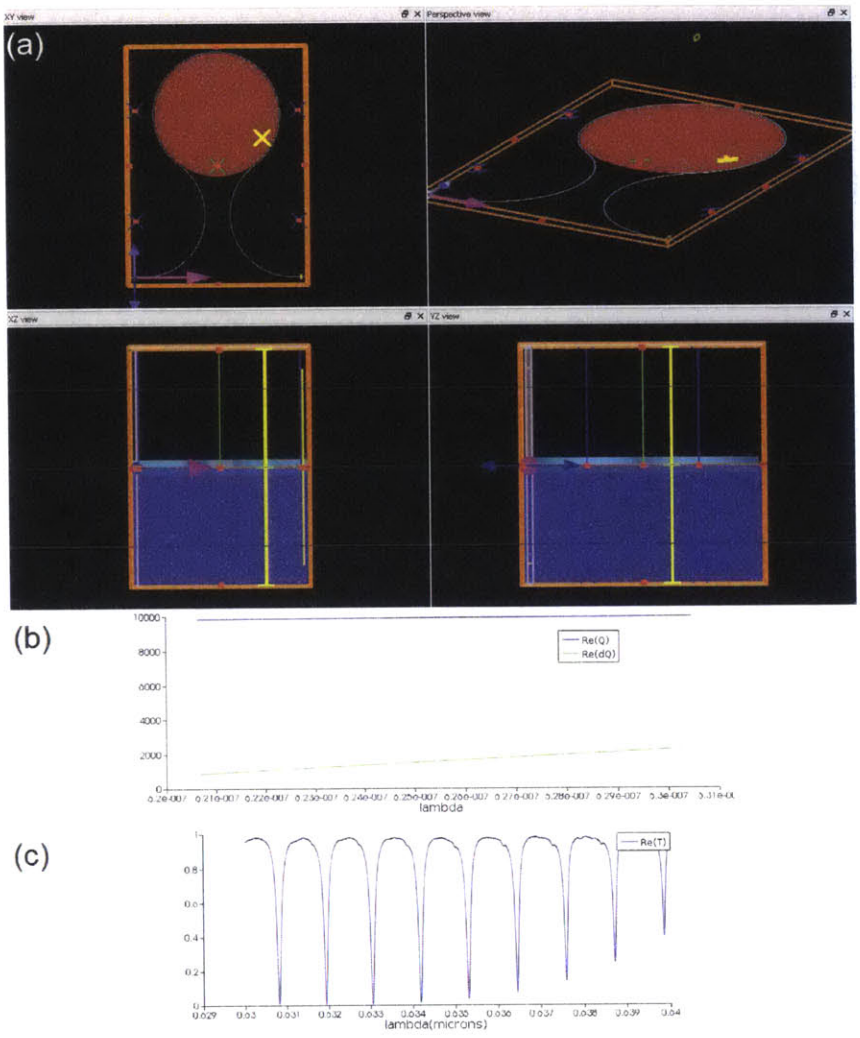

Figure 4-9: (a) Simulation setup for a disk resonator of 30 μm coupled to one bus waveguide by a coupling length of 150 μm and coupling gap of 200 nm. The input port is at the bottom left and the through port is at the bottom right. (b) Spectrum of the Q factor of the disk as a function of wavelength. (c) Transmission spectrum of the through port.

very close to 0. In addition, Figure 4-9(b) shows that the Q of the microdisk indeed is 10,000.

4.3.3 Plans for Better Design

Although we do get a design for critically coupling a waveguide to a microdisk with radius of 30 μm, this leaves no room for the drop bus waveguide. After studying

this wrap-around coupling scheme a bit more, we realized that unlike a single point coupling, it is necessary to match the phase of the waveguide and the phase of the microdisk cavity. If somehow there is a phase mismatch of a multiple of π, the coupling vanishes even if there is a strong field overlap [11]. The phase matching condition is dependent on the gap, waveguide width, and mode of the microdisk resonator. We could also consider using a multi-mode interference (MMI) coupler to couple from the waveguide to the microdisk. This is currently an on-going study for this project.

4.4 Directional Coupler for 50:50 Split

4.4.1 Analytical Calculations

A crucial component of a Mach Zehnder Interferometer is the directional coupler with 50:50 splitting ratios. Directional couplers are straight sections of two waveguides where the evanescent modes of one waveguide overlap with the modes of the second waveguide. As a result, light from one waveguide slowly transfers back and forth to the second waveguide. The fraction of light from one waveguide that is transferred to the other waveguide is a function of the distance between the two waveguides and the length of the coupling region. For our directional coupler, we chose the coupling gap to be 100 nm so that there is a sufficient amount of overlap of the evanescent modes of one waveguide with the modes of the second waveguide. To get a first order estimate of the coupling length necessary to create a 50:50 splitting ratio, we use Lumerical's MODE Solutions eigenmode solver to find the difference in index between the two supermodes of the waveguide structure, which are known as the symmetric and antisymmetric supermodes.

Figure 4-10 shows these results, where Figure 4-10(a) is the simulation setup, Figure 4-10(b) is the real part of the Ey modal field of the symmetric supermode with effective index of 1.816090, and Figure 4-10(c) is the real part of the Ey modal field of the antisymmetric supermode with effective index of 1.810253. From these two values, we can use analytical formulas to calculate the necessary coupling length

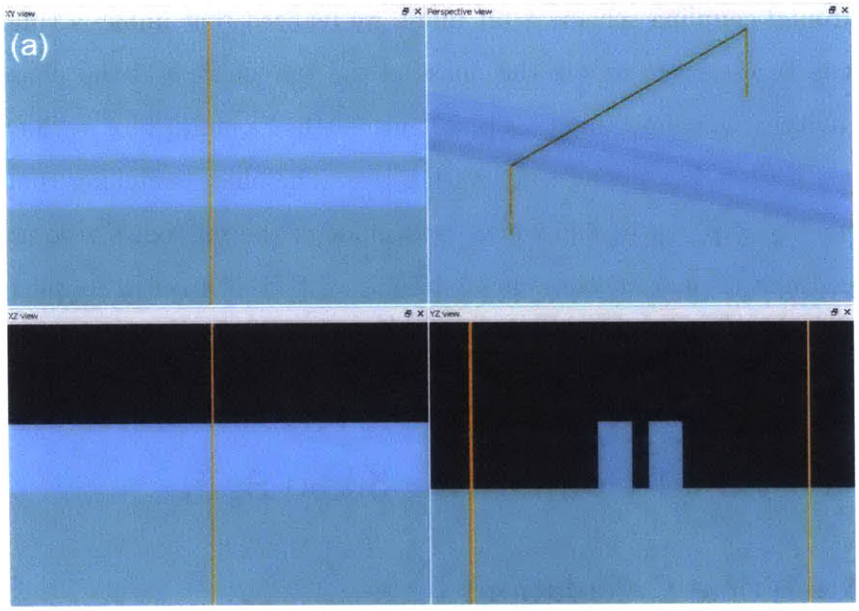

(b)

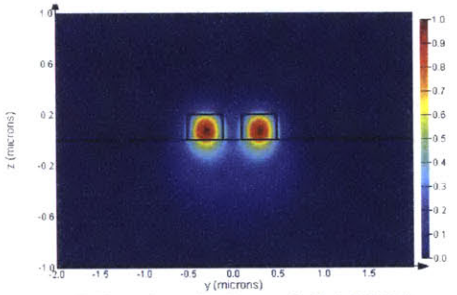

Effective Index: 1.816090

(c)

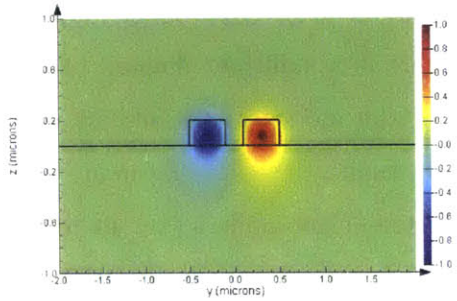

Effective Index: 1.810253

Figure 4-10: (a) Simulation setup for solving the eigenmode of two straight waveguides coupled evanescently to each other. (b) Real part of the Ey modal field of the symmetric supermode. (c) Real part of the Ey modal field of the antisymmetric supermode.

to achieve 50:50 splitting ratios. Let us assume we have 100% of the power initially

in waveguide 1. Then, after the light from waveguide 1 passes through a directional coupler of length L between waveguide 1 and waveguide 2, the power of light that is now in waveguide 2 is given by:

$$P_2(L) = P_0 \sin^2\left(\frac{\pi L \Delta n}{\lambda_0}\right) \tag{4.6}$$

where Δn is the index difference between the symmetric and antisymmetric supermodes, L is the length of the coupling region, P_0 is the input power, and λ_0 is the free space wavelength. Hence, if we manipulate Equation (4.6), we can calculate the coupling length necessary to achieve any desired power coupling to waveguide 2:

$$L = \frac{\lambda_0}{\pi \Delta n} \sin^{-1}\left(\sqrt{\frac{P_2}{P_0}}\right) \tag{4.7}$$

Therefore, if we want 50% of the light from waveguide 1 to couple into waveguide 2, then we need the following length:

$$L = \frac{0.637\mu m}{\pi(1.816090 - 1.810253)} \sin^{-1}\left(\sqrt{\frac{0.5}{1}}\right) = 27.283\mu m \tag{4.8}$$

4.4.2 Variational FDTD Simulations

In order to test the accuracy of our analytical results from (4.8), we did an optimization for finding the necessary 50:50 splitting ratios of the directional coupler using Lumerical's 2.5D FDTD Propagation Method. This variational FDTD solver efficiently simulates the propagation of light in a guided structure. This is a good first set of simulations since it is faster than the highly computationally intensive three-dimensional FDTD method for solving large photonic structures, which is what we have in this case since the coupling length is required to be 27.283 μm. For these simulations, we assume that the waveguide bend that guides the two separate waveguides to the directional coupler section is 20 μm since AlN has a small index contrast with air surrounding the structures, so we use a large bend radius to reduce propagation loss. When doing the optimization using the 2.5D variational FDTD solver, we

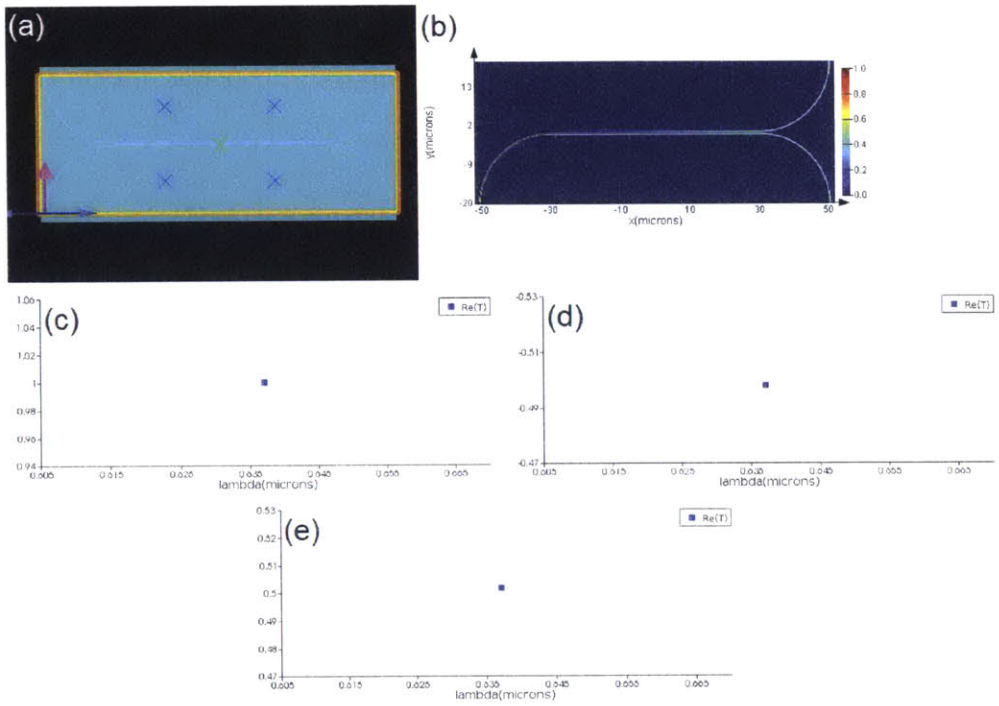

Figure 4-11: (a) 2.5D variational FDTD simulation setup for solving the splitting ratio of a directional coupler with bend radius of 20 μm and coupling length of 60.673 μm. Bottom left hand is the location of the input mode of waveguide 1, bottom right hand is the location of the output mode of waveguide 1, and the top right hand is the location of the output mode of waveguide 2. (b) Electric field profile of the entire propagation structure. (c) Transmission of power through the waveguide 1 input. (d) Transmission of power through the waveguide 1 output. (e) Transmission of power through the waveguide 2 output.

found that 60.673 μm is actually the coupling length that results in a 50:50 splitting ratio, as seen in Figure 4-11. We see in Figure 4-11(b) that the electric field profile of the entire propagation structure has equal power splitting at the waveguide 1 and waveguide 2 outputs. Figures 4-11(d) and (e) show the transmission of the power through the waveguide 1 output and the waveguide 2 output, respectively, to confirm that indeed there is a splitting of 50:50 of the power of light inserted at the waveguide 1 input shown in Figure 4-11(c).

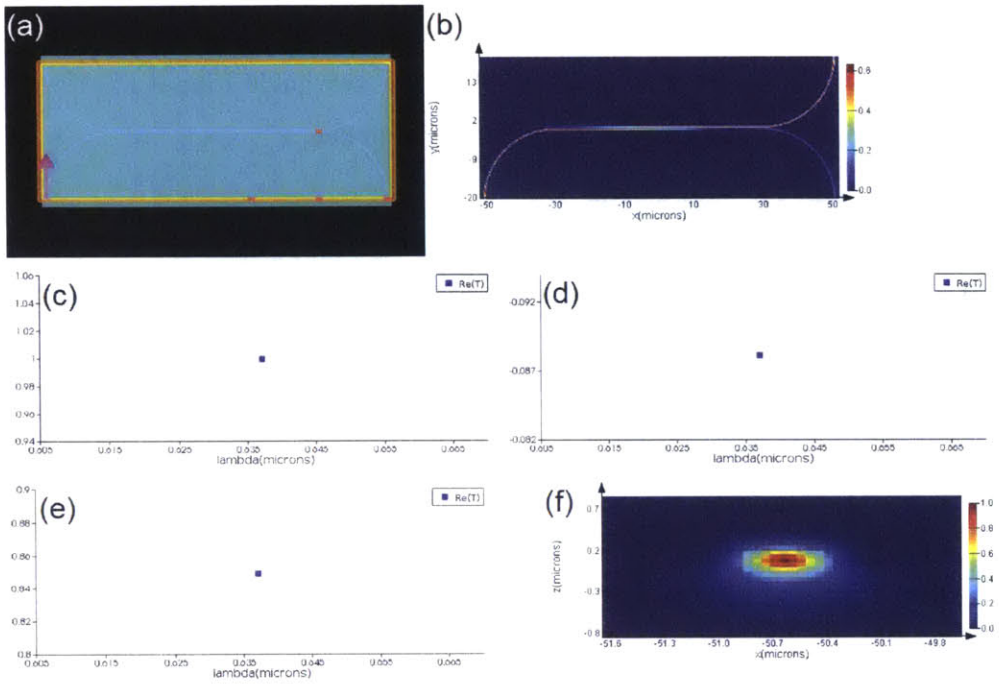

Figure 4-12: (a) 3D FDTD simulation setup for solving the splitting ratio of a directional coupler with bend radius of 20 μm and coupling length of 60.673 μm. Bottom left hand is the location of the input mode of waveguide 1, bottom right hand is the location of the output mode of waveguide 1, and the top right hand is the location of the output mode of waveguide 2. (b) Electric field profile of the entire propagation structure. (c) Transmission of power through the waveguide 1 input. (d) Transmission of power through the waveguide 1 output. (e) Transmission of power through the waveguide 2 output. (f) Electric field mode profile of the waveguide 1 input.

4.4.3 3D FDTD Simulations

Since there is a large discrepancy between the analytical calculations and the Lumerical 2.5D variational FDTD results, we also analyzed the structure in Figure 4-11(a) using the Lumerical's 3D FDTD. This is the most accurate simulation that can be run, though it is highly computationally intensive and takes a few days to run. Figure 4-12 shows the result of the 3D FDTD simulation that was performed on the exact same structure as the one shown in Figure 4-12(a). We see in Figure 4-12(b) that the electric field profile of the entire propagation structure does not have equal power splitting at the waveguide 1 and waveguide 2 outputs. Figures 4-12(d) and (e) show the transmission of the power through the waveguide 1 output and the waveguide 2

output, respectively, to confirm that indeed the splitting is not 50:50, rather it is 85:9. Figures 4-12(f) is the electric field mode profile of the waveguide 1 input to show that we are exciting the waveguide's fundamental single mode.

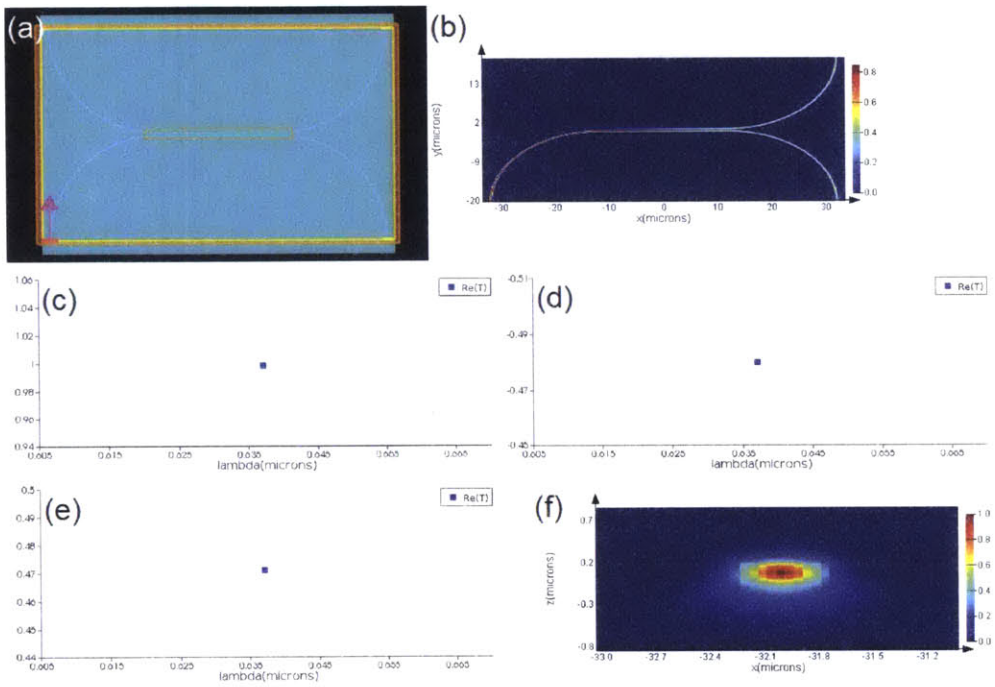

Figure 4-13: (a) 3D FDTD simulation setup for solving the splitting ratio of a directional coupler with bend radius of 20 μm and coupling length of 23.43 μm. Bottom left hand is the location of the input mode of waveguide 1, bottom right hand is the location of the output mode of waveguide 1, and the top right hand is the location of the output mode of waveguide 2. (b) Electric field profile of the entire propagation structure. (c) Transmission of power through the waveguide 1 input. (d) Transmission of power through the waveguide 1 output. (e) Transmission of power through the waveguide 2 output. (f) Electric field mode profile of the waveguide 1 input.

Figure 4-13 shows the optimization for finding the necessary 50:50 splitting ratios using Lumerical's 3D FDTD. We found that 23.43 μm is actually the coupling length that results in a 50:50 splitting ratio. We see in Figure 4-13(b) that the electric field profile of the entire propagation structure has equal power splitting at the waveguide 1 and waveguide 2 outputs. Figures 4-13(d) and (e) show the transmission of the power through the waveguide 1 output and the waveguide 2 output, respectively, to confirm that indeed there is a splitting of 50:50 of the power of light inserted at the waveguide

1 input shown in Figure 4-13(c). Figures 4-13(f) is the electric field mode profile of the waveguide 1 input to show that we are exciting the waveguide's fundamental mode. The result of this simulation is in agreement with our analytical calculations. In our analytical calculations, we assumed that the waveguide 1 is coupled to waveguide 2 abruptly by the directional coupler. However, in the 3D FDTD simulations, we feed the directional coupler with waveguide bends since introducing a second waveguide abruptly usually results in scattering. As such, in the waveguide bend section, there is already some evanescent coupling between the two waveguides, which makes the necessary coupling length slightly shorter than the analytical results.

Chapter 5

In-House Fabrication and Fast Prototyping

In the nascent stages of a long-term project such as this, it is necessary to have the capability of fabricating simple passive structures in-house in order to optimize designs. Otherwise, multi-project runs typically take 6 months to produce a chip, which is not ideal when testing simple photonic structures in the beginning. In this section, I will go over the repeatable and high-quality fabrication procedure I developed using MIT's Microsystems Technology Laboratories for making devices that we can test. This capability will allow us to quickly make chips in less than a day, test, and repeat for better and better optimizations. For our fast prototyping, we will be using 200 nm of AlN on top of sapphire wafers, which we purchased from Kyma Technologies. The side view of the aluminum nitride on sapphire wafers is shown in Figure 5-1.

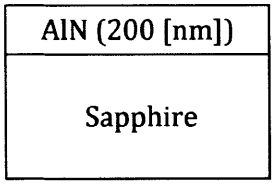

Figure 5-1: Starting substrate of the aluminum nitride on sapphire wafers.

5.1 First Generation Test Structures

For our first generation test structures, we want to check the AlN waveguide propagation loss, as well as the splitting ratio of the directional coupler. This is important to test to see how good the fabrication process is, in addition to serving as the basis for testing other photonic structures in the future, like Distributed Bragg Reflector filters and microdisk resonator filters. Figure 5-2 shows the structure for testing waveguide loss where we have a short waveguide section and two grating couplers on each side for coupling light into and out of the waveguide. Figure 5-3 shows the structure for testing the directional coupler splitting.

Figure 5-2: Structure for testing waveguide loss.

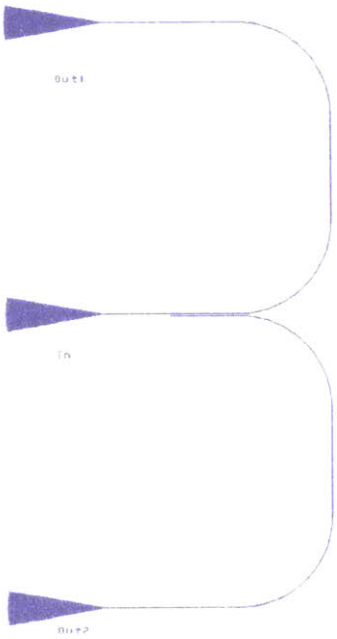

Figure 5-3: Structure for testing directional coupler splitting.

5.1.1 Grating Couplers

An important component for the first generation test structures is the grating couplers. Although for the final product of the programmable nanophotonic processor we will do routing and detection of the NV emission all on-chip to minimize propagation loss, we need to use either grating couplers or edge couplers to couple light into the AlN waveguide circuit during the prototyping stages to test each component. Although edge couplers (or end-fire couplers) would be better since they have been shown to have greater than 90% coupling efficiency, grating couplers are much easier to make and can be placed anywhere on the chip, which is better for first generation devices. However, we are in the process of incorporating edge couplers for future test structures.

Grating couplers operate by taking advantage of the Bragg condition to scatter light out of plane at each unit cell of the periodic grating. Using the Bragg condition analytical equation, we can find the grating period for coupling light into and out of the chip:

$$\sin(\theta) = \frac{n_{eff} - \frac{m\lambda}{a}}{n_{cladding}} \tag{5.1}$$

where θ is the angle of the emission from the grating coupler when coupling light from a waveguide out of plane, n_{eff} is the effective waveguide index of the grating, $n_{cladding}$ is the index above the waveguide, λ is the wavelength of light we are interested in, a is the pitch of the grating, and m can take on any value. Typically $m = 1$ to not send out light at many different angles, but rather at only one particular angle (only one order of light). We can manipulate the Bragg condition analytical equation to get the grating pitch we need:

$$a = \frac{\lambda}{n_{eff} - \sin(\theta) n_{cladding}} \tag{5.2}$$

We will arbitrary choose θ to be 13.45 degrees and $n_{cladding}$ to equal 1 since we will not cap the AlN waveguide with anything. n_{eff} can be calculated by finding the

effective indices of the etched and unetched portion of each unit cell of the grating coupler by using the Lumerical eigenmode solver in MODE solutions. Then, n_{eff} is approximately the average of the two effective indices. We designed these grating couplers for both 532 nm light and 637 nm light.

In the case of 532 nm light, the effective index of the unetched portion is 2.005 and the etched portion is simply the air cladding since we will be using gratings in which the etched portion is etched all the way to the bottom substrate. Hence, the pitch should be the following in order to operate the way we want it to:

$$a = \frac{0.532\mu m}{(2.005+1)/2 - \sin(13.45)(1)} = 0.419\mu m \tag{5.3}$$

In the case of 637 nm light, the effective index of the unetched portion is 1.96 and the etched portion is simply the air cladding since we will be using gratings in which the etched portion is etched all the way to the bottom substrate. Hence, the pitch should be the following in order to operate the way we want it to:

$$a = \frac{0.637\mu m}{(1.96+1)/2 - \sin(13.45)(1)} = 0.511\mu m \tag{5.4}$$

These grating designs were simulated using Lumerical's 2D FDTD by testing the coupling from a waveguide source to out of the plane and by testing the coupling of a beam from a Gaussian source into the waveguide mode. We found that for both gratings, these values are around 25% to 35%. For the final grating coupler design, we made the grating circular and tapered it from a 30 μm wide section to the 1 μm wide waveguide.

5.2 Fabrication

Developing a reliable and repeatable in-house fabrication procedure was by far the most difficult and time-consuming portion of this project. I experimented extensively in trying to find the best electron beam resist and dry etch recipe to use.

To start off, I used ZEP520A as my resist, but I found that I would need over

800 nm thick ZEP520A to withstand the dry etch. I also tried using CF_4/Ar etch chemistry, as well as Cl_2/BCl_3/Ar etch chemistry. I found that Cl_2/BCl_3/Ar etch chemistry is not good for ZEP520A since it creates a build-up of material at etch edges that cannot be removed, even with piranha. CF_4/Ar does not have this problem, but the ZEP520A etch resistivity is worst in CF_4/Ar than in Cl_2/BCl_3/Ar, so it actually requires more than 1000 nm thick ZEP520A to withstand the dry etch. It is not ideal to use such a thick resist since the resolution would be much worse.

Then, I moved on to using HSQ for the electron beam resist mask since HSQ becomes similar to SiO_2 after development, which is much hardier against dry etching. I found that HSQ has a better etch resistivity in Cl_2/BCl_3/Ar etch than in CF_4/Ar. Specifically, only 130 nm of HSQ is required for etching 200 nm of AlN, while 450 nm of HSQ is not even enough to etch 140 nm of AlN. This is expected since CF_4/Ar is typically used for etching SiO_2. Since the bottom substrate is sapphire for the AlN wafers, I developed a novel fabrication process for removing the HSQ after fabrication while keeping the underlying sapphire layer unharmed, which is highlighted in the following:

1. Clean small 5 mm by 5 mm unpatterned chips with sonication in acetone, methanol, and isopropyl alcohol, consecutively, for 5 minutes each.

2. Use the ebeam evaporator to evaporate 25 nm of Cr on top of the AlN layer at a rate of 1 Å/s.

3. Oxygen plasma etch the Cr layer for 1 minute and 100 W power.

4. Spin coat HSQ FOX-16 electron beam resist at 5000 rpm for 1 minute, then bake at 80°C for 4 minute. This results in about 425 nm of HSQ film as resist mask. HSQ is used since it has good resolution and high contrast and it has a better etch resistance than ZEP520A and PMMA.

5. Use the Elionix ebeam writer to pattern the resist, using about 9600 $\mu C/cm^2$ dose to clear.

6. Develop in salty developer (1 wt% NaOH and 4 wt% NaCl) for 4 minutes, followed by 10 minute rinse in DI water to stop development. Then, immerse in methanol for 1 minutes, followed by air drying to not damage the structures. The salty developer was formulated by Yang et al. in 2007 [27], and it was shown to help greatly improve the resolution of HSQ masks.

7. Dry etch through the 25 nm Cr layer using Plasmaquest ECR-RIE, using a Cl_2/O_2 dry etch chemistry. After this step, the side view of the chip looks like the following:

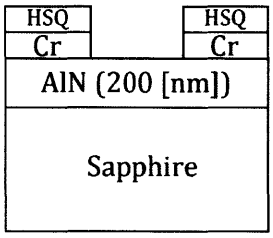

Figure 5-4: Side view of chip after HSQ patterning and Cr dry etch.

8. Dry etch through the 200 nm AlN layer using SAMCO ICP-RIE, using a $Cl_2/BCl_3/Ar$ dry etch chemistry.

9. Remove HSQ layer by immersing the chip face down in a funnel in a Cr-7 (chrome etchant) bath for 1 hour. Then, flip the chip right side up in the Cr-7 bath and place the bath in a sonicator for 10 minutes.

10. Rinse the chip in DI water for 5 minute to wash away the Cr-7. Then, immerse in methanol for 1 minute, followed by air drying to not damage the structures.

It is also possible to remove the HSQ with HF without etching the sapphire, so the steps involving Cr as a liftoff layer can be skipped as well.

Figures 5-5, 5-6, and 5-7 show the microscope images of the finished product of the AlN chip fabrication. Figure 5-8 shows an atomic force microscope scan of a portion of the AlN waveguide to demonstrate that the AlN layer is etched all the way

through and the structures are quite pristine with fairly straight sidewalls. Figures 5-9 shows an atomic force microscope scan of an AlN grating coupler. It might seem that the gratings are not etched all the way through and that the sidewalls are not very straight, but that is an artifact of the AFM scan. The AFM scans show that the etch depth is about 220 nm to 230 nm, which is within the thickness uniformity of 200 nm +/- 10% the wafers are rated at.

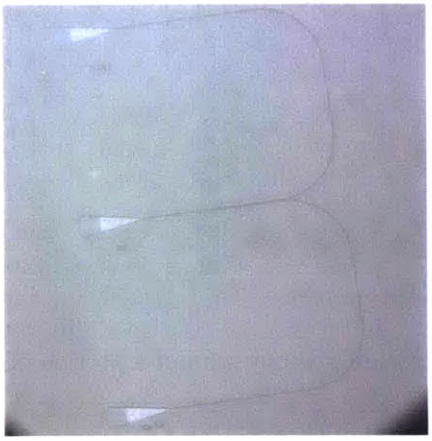

Figure 5-5: 50x microscope image of structure for testing directional coupler splitting.

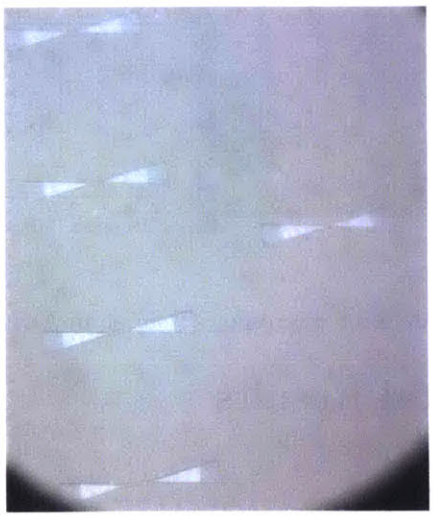

Figure 5-6: 50x microscope image of structure for testing waveguide loss.

Figure 5-7: 100x microscope image of structure for testing waveguide loss.

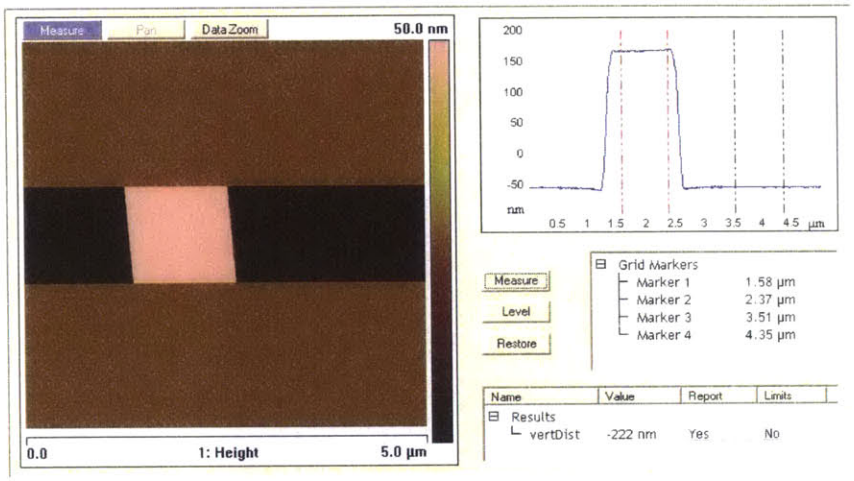

Figure 5-8: Atomic force microscopy scan of a portion of the AlN waveguide.

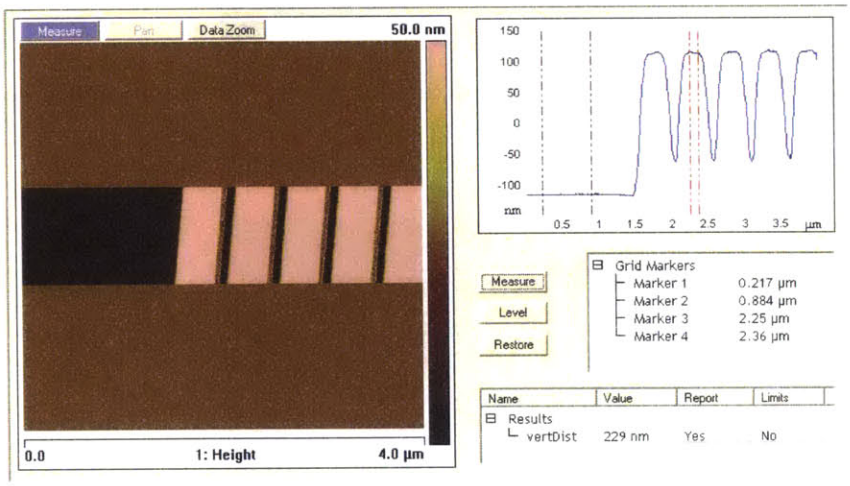

Figure 5-9: Atomic force microscopy scan of an AlN grating coupler.

5.3 Experimental Results

5.3.1 Confocal Setup

For testing the AlN chips, we use a confocal microscope setup similar to the one shown in Section 2.5.1, except the setup uses optical elements that are made for

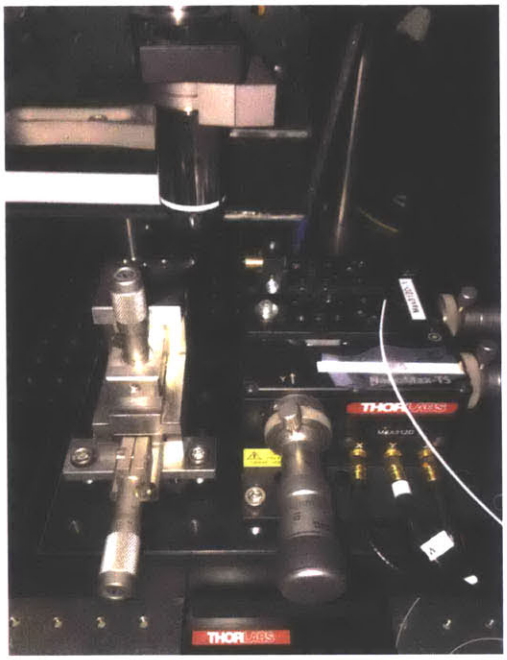

Figure 5-10: Picture of the sample stage portion of the experimental setup, where the left stage is the sample stage and the right Thorlabs stage is the piezo stage for positioning the fiber.

visible wavelengths and the sample is mounted on a translational stage rather than in a cryostat. This means that the confocal microscope setup does not have translational stages for moving the optics with respect to the sample. Also, we use a lensed fiber to pump light into the input grating coupler, while using the confocal microscope to collect the light from the output grating coupler. The fiber has its own translational stage for adjusting its position with respect to the AlN chip. Figures 5-10 shows the Thorlabs piezo stage for positioning the fiber with high precision on the right and the sample stage on the left, right underneath the objective. The sample stage is really only for moving the sample up and down, or in and out of focus. Both of these stages sit on top of another large translational stage so that once the ideal positioning of the fiber is obtained with respect to the sample stage, the sample can be moved around without perturbing its position with respect to the fiber.

5.3.2 Confocal Microscopy Experiments

For the confocal microscopy experiments, we first move the large translational stage so that the confocal microscope objective is right above the location of the input grating coupler. From there, we can see the input grating coupler on our white light illumination field of view, as well as the excitation spot from the fiber. We tune the position of the fiber until the excitation spot is entirely in the grating section of the input grating coupler. Then, we move the large translational stage so that we are viewing the output grating coupler on our white light illumination field of view. To confirm the confocal scan encompasses the grating coupler, we excite with a 532 nm laser and collect the reflection using the confocal microscope. The result is shown in Figure 5-11.

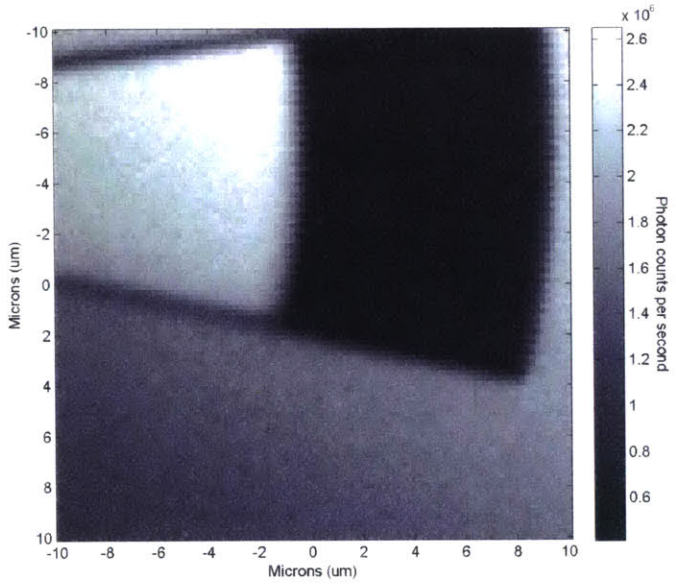

Figure 5-11: Region of the output grating coupler in the confocal scan window. Image is taken by exciting and collecting the reflection using the confocal microscope.

Afterwards, we excite with a 532 nm laser using the fiber so that light is pumped at the input grating coupler. This time, we collect the light from the output grating by using the confocal microscope. The result is shown in Figure 5-12. We do not see any significant bright scattering at the grating region, which leads us to believe there

is something wrong with the test structures or with our experimental setup.

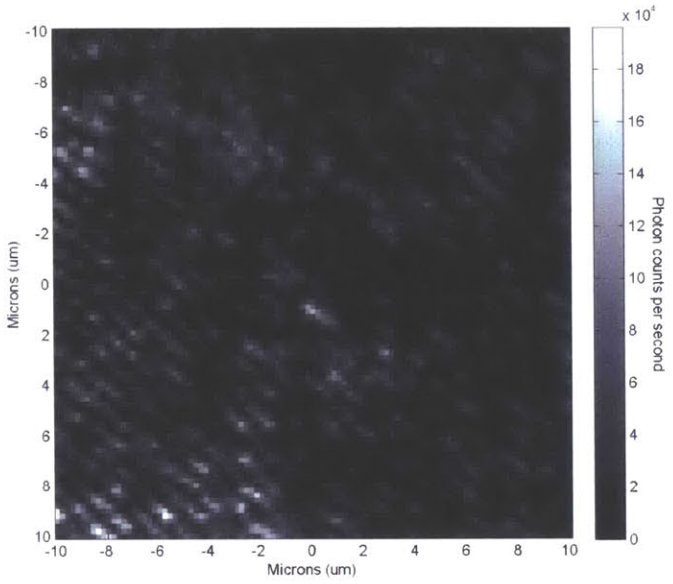

Figure 5-12: Confocal scan when pumping with the fiber at the input grating and collecting the light from the output grating by using the confocal microscope.

One room for improvement is to look at the design of the grating couplers once again. It would be good to simulate the input grating using the exact specifications of the lensed fiber and to simulate the output grating using the exact specifications of the objective. In addition, I should look at extending the simulation to 3D FDTD simulations in order to optimize the tapering section as well. Furthermore, the grating couplers being designed and fabricated now have grating etches that goes all the way through the AlN and stops at the sapphire substrate. However, the best grating couplers designed in silicon photonics often use partial etches since that is much better at scattering the incident light out of plane. The downside of this is that the fabrication usually requires two lithography steps. The plan would be to use a fabrication trick demonstrated by Sapienza et al. in their 2015 Nature Communications paper that would allow two different etch depths from just a single lithography step [20].

We can also improve our experimental setup by using a lower NA lensed fiber for pumping light into the input grating coupler. The reason is that the grating couplers

were designed with $m = 1$ so that light is not send out at many different angles, but rather at only one particular angle. This applies to the input as well. Hence, for the coupling to be more efficient, it would be best to use a lower NA lensed fiber that is coupling light at a smaller range of angles into the grating coupler. The same would apply for the objective at the output grating, so we should look into using a lower NA objective as well.

Chapter 6

Conclusions and Future Work

In this thesis, we demonstrated efforts toward building a fiber-integrated single photon source based on InAs epitaxially grown quantum dots, as well as building a quantum repeater using nitrogen vacancy centers as quantum memories and AlN nanophotonic devices as a wide-bandgap programmable nanophotonic processor. All these efforts are steps toward the direction of building efficient light-matter interfaces for modular quantum systems.

For the fiber-integrated single photon source, we have shown promising designs for the device architecture, as well as a dependable and repeatable fabrication process for making the bullseye membranes. In addition, we were able to get promising spectroscopy experiments using a scanning confocal microscope that has optical access into the cryostat where the QD experiments were performed. The enhanced emission of QDs in the bullseye structure and the fact that the bullseye spectrum matched up closely with simulations show that the device fabrication was indeed very good. However, more work has to be done on the experimental setup in order to characterize the devices further and to determine if we have a QD that is aligned perfectly spatially and spectrally to a bullseye structure. Then, we will need to pick-and-place these structures onto a fiber facet and test to see if we do get a significantly higher-rate of single photon production in this plug-and-play single photon source. Our plan is to also extend this work to NVs in an attempt to demonstrate record-high photon collection rate from a single NV center by integrating the bullseye structure with an

NV in it to the facet of a high NA fiber.

For the quantum repeater using nitrogen vacancy centers as quantum memories and AlN programmable nanophotonic processor, we highlighted a long-term effort with Sandia National Laboratories, as well as short-term efforts to demonstrate the efficient routing and detection of photons from NVs in AlN photonic circuits. We showed that using the tools in our arsenal, we can design all the necessary components for the Mach-Zehnder Interferometer array. In addition, we were successful in developing a repeatable and high-quality fabrication process at MIT for making AlN devices for fast prototyping and optimization. Our immediate future goal is to come up with a good way for coupling light into and out of the AlN chip for testing our structure, whether it is to develop better grating couplers or proceed with a collaboration to integrate edge couplers. We hope to get a baseline value for the device testing, so that we have a starting point to improve upon over the next few years. Our vision is to one day create these quantum repeaters for aiding in the experimental demonstrations of various quantum information processing and quantum communication protocols.

Bibliography

[1] S. Ates, L. Sapienza, M. Davanco, A. Badolato, and K. Srinivasan. Bright single-photon emission from a quantum dot in a circular bragg grating microcavity. *IEEE Journal Of Selected Topics in Quantum Electronics*, 18:1711–1721, 2012.

[2] T. Babinec, B. Hausmann, M. Lhan, Y. Zhang, J. Maze, P. Hemmer, and M. Loncar. A diamond nanowire single-photon source. *Nature Nanotechnology*, 5:195–199, 2010.

[3] H. Bernien, B. Hensen, W. Pfaff, G. Koolstra, M. Blok, L. Robledo, T. Taminiau, M. Markham, D.d Twitchen, L. Childress, and R. Hanson. Heralded entanglement between solid-state qubits separated by three metres. *Nature*, 497:86–90, 2013.

[4] L. Chrostowski and M. Hochberg. chapter 4, pages 91–141. Cambridge University Press, 1st edition, 2015.

[5] M. Davanco, M. T. Rakher, D. Schuh, A. Badolato, and K. Srinivasan. A circular dielectric grating for vertical extraction of single quantum dot emission. *Applied Physics Letters*, 99:041102, 2011.

[6] M. W. Doherty, N. B. Manson, P. Delaney, F. Jelezko, J. Wrchtrup, and L. C. L. Hollenberg. The nitrogen-vacancy colour centre in diamond. *Physics Reports*, 528:1–45, 2013.

[7] M. V. Gurudev Dutt, L. Childress, L. Jiang, E. Togan, J. Maze, F. Jelezko, A. S. Zibrov, P. R. Hemmer, and M. D. Lukin. Quantum register based on individual electronic and nuclear spin qubits in diamond. *Science*, 316:1312, 2007.

[8] D. Englund, D. Fattal, E. Waks, G. Solomon, B. Zhang, T. Nakaoka, Y. Arakawa, Y. Yamamoto, and J. Vuckovic. Controlling the spontaneous emission rate of single quantum dots in a two-dimensional photonic crystal. *Physical Review Letters*, 95:013904, 2005.

[9] A.L. Falk and D.D. Awschalom. Spins charge ahead. *Nature Photonics*, 7:510–511, 2013.

[10] M. R. Foreman and P. Torok. *New Journal of Physics, Pages = , Title = Spin-orbit coupling and conservation of angular momentum flux in non-paraxial imaging of forbidden radiation, Volume = 13, Year = 2011.*

[11] E. S. Hosseini, S. Yegnanarayanan, and A. H. Atabaki. Systematic design and fabrication of high-q single-mode pulley-coupled planar silicon nitride microdisk resonators at visible wavelengths. *Optics Express*, 18:2127–2136, 2010.

[12] L. Li, E. H. Chen, J. Zheng, S. L. Mouradian, F. Dolde, T. Schroder, S. Karaveli, M. L. Markham, D. J. Twitchen, and D. Englund. Efficient photon collection from a nitrogen vacancy center in a circular bullseye grating. *Nano Letters*, 15:1493–1497, 2015.

[13] P. C. Maurer, G. Kucsko, C. Latta, L. Jiang, N. Y. Yao, S. D. Bennett, F. Pastawski, D. Hunger, N. Chisholm, M. Markham, D. J. Twitchen, J. I. Cirac, and M. D. Lukin.

[14] S. L. Mouradian, T. Schroder, C. B. Poitras, L. Li, J. Goldstein, E. H. Chen, J. Cardenas, M. L. Markham, D. J. Twitchen, M.l Lipson, and D. Englund. Scalable integration of long-lived quantum memories into a photonic circuit. *arXiv:1409.7965v2*, 2014.

[15] F. Najafi, J. Mower, N. C. Harris, F. Bellei, A. Dane, C. Lee, X. Hu, P. Kharel, F. Marsili, S. Assefa, K. K. Berggren, and D. Englund. On-chip detection of non-classical light by scalable integration of single-photon detectors. *Nature Communications*, 6, 2015.

[16] P. Neumann, N. Mizuochi, F. Rempp, P. Hemmer, H. Watanabe, S. Yamasaki, V. Jacques, T. Gaebel, F. Jelezko, and J. Wrachtrup. Multipartite entanglement among single spins in diamond. *Science*, 320:1336, 2008.

[17] R. Patel, T. Schroder, N. Wan, L. Li, S. L. Mouradian, E. H. Chen, and D. Englund. Efficient photon coupling from a diamond nitrogen vacancy centre by integration with silica fibre. *arXiv:1502.07849v1*, 2015.

[18] W. Pfaff, B. Hensen, H. Bernien, S. B. van Dam, M. S. Blok, T. H. Taminiau, M. J. Tiggelman, R. N. Schouten, M. Markham, D. J. Twitchen, and R. Hanson. Unconditional quantum teleportation between distant solid-state quantum bits. *Science*, 345:532–535, 2014.

[19] J. Riedrick-Moller, L. Kipfstuhl, C. Hepp, E. Neu, C. Pauly, F. Mucklich, A. Baur, M. Wandt, S. Wolff, M. Fischer, S. Gsell, M. Schreck, and C. Becher. One- and two-dimensional photonic crystal microcavities in single crystal diamond. *Nature Nanotechnology*, 7:69–74, 2012.

[20] L. Sapienza, M. Davanco, A. Badalato, and K. Srinivasan. Nanoscale optical positioning of single quantum dots for bright and pure single-photon emission. *Nature Communications*, 6, 2015.

[21] S. Strauf, N. G. Stoltz, M. T. Rakher, L. A. Coldren, P. M. Petroff, and D. Bouwmeester. High-frequency single-photon source with polarization control. *Nature Photonics*, 1:704–708, 2007.

[22] J. M. Taylor, P. Cappellaro, L. Childress, L. Jiang, D. Budker, P. R. Hemmer, A. Yacoby, R. Walsworth, and M. D. Lukin. High-sensitivity diamond magnetometer with nanoscale resolution. *Nature Physics*, 4:810–816, 2008.

[23] E. Togan, Y. Chu, A. Trifonov, L. Jiang, J. Maze, L. Childress, M. G. Dutt, A. S. Soorensen, P. Hmmer, A. Zibrov, and M. D. Lukin. Quantum entanglement between an optical photon and a solid-state spin qubit. *Nature*, 466:730–734, 2010.

[24] Wikipedia. Exciton energy levels, 2011.

[25] J. Wolters, N. Sadzak, A. W. Schell, T. Schroder, and O. Benson. Ultrafast spectral diffusion measurement on nitrogen vacancy centers in nanodiamonds using correlation interferometry. *arXiv:1206.0852v3*, 2012.

[26] C. Xiong, W. H. P. Pernice, X. Sun, C. Schuck, K. Y. Fong, and H. X. Tang. Aluminum nitride as a new material for chip-scale optomechanics and nonlinear optics. *New Journal of Physics*, 14:095014, 2012.

[27] J. K. W. Yang and K. K. Berggren. Using high-contrast salty development of hydrogen silsesquioxane for sub-10-nm half-pitch lithography. *Journal of Vacuum Science and Technology B*, 25:2025–2029, 2007.